Environmental Modelling and Software 185 (2025) 106303

Contents lists available at ScienceDirect

Environmental Modelling and Software

journal homepage: www.elsevier.com/locate/envsoft

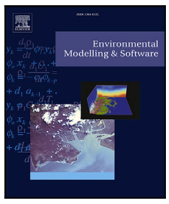

Position Paper

Modelling wildfire spread and spotfire merger using conformal mapping and AAA-least squares methods

Samuel J. Harris *, N.R. McDonald

Department of Mathematics, University College London, Gower Street, London, WC1E 6BT, United Kingdom

ARTICLE INFO

Keywords:
Wildfire modelling
Free boundary problems
Fluid dynamics
Conformal mapping
AAA-least squares algorithm
Fire spread

ABSTRACT

A two-dimensional model of wildfire spread and merger is presented. Three features affect the wildfire propagation: (i) a constant basic rate of spread term accounting for radiative and convective heat transfer, (ii) the unidirectional, constant ambient wind, and (iii) a fire-induced pyrogenic wind. Two numerical methods are proposed to solve for the pyrogenic potential. The first utilises the conformal invariance of Laplace's equation, reducing the wildfire system to a single Polubarinova–Galin type equation. The second method uses a AAA-least squares method to find a rational approximation of the pyrogenic potential. Various wildfire scenarios are presented and the effects of the pyrogenic wind and the radiative/convective basic rate of spread terms investigated. Firebreaks such as roads and lakes are also included and solutions are found to match well with existing numerical and experimental results. The methods proposed in this work are suitably fast and new to the field of wildfire modelling.

Software and data availability

The codes that were used, and the resulting data produced, in this work for calculating the wildfire spread and spotfire merger were created using the MATLAB programming language (version R2024a) and can be found in the following Github repository: https://github.com/Sam-J-Harris/wildfire_spread_spotfire_merger. This repository was created by Samuel Harris (e-mail: sam.harris.16@ucl.ac.uk) and contains all MATLAB code used (8.26MB) and data produced (154MB). Author's experimental environment was as follows:

- OS: Windows 11
- CPU: 11th Gen Intel(R) Core(TM) i7-1185G7 @ 3.00GHz
- RAM: 32.00 GB
- GPU: Intel(R) Iris(R) Xe Graphics

The data produced in this work is also made publicly available at the above Github link. Data for all figures can be found in the '00 Data' folder in the form of .mat (boundary data for the evolving fire lines) and .fig (images of the fire line evolution) files. The only other data used in this work were images of the experimental fires detailed in Sullivan et al. (2019) and the numerical outputs of Hilton et al. (2018). This data was provided to us by the authors of these papers.

1. Introduction

1.1. The global wildfire challenge

Climate change predictions indicate a continued, substantial shift in global weather. Fire weather conditions, as defined in e.g. Jolly et al. (2015), are forecast to increase worldwide over the coming decades which would result in an enhanced level of 'fire danger' and an increased risk of catastrophic wildfire development (Arnell et al., 2021; Masson-Delmotte et al., 2021; Hetzer et al., 2024). The growing prevalence of wildfires is now a global phenomenon with large, dynamic wildfires – so called mega fires – increasing in frequency and intensity worldwide (Attiwill and Binkley, 2013). Wildfire research, specifically that involving the complex and nonlinear dynamics and thermodynamics associated with wildland fire spread, is consequently receiving growing attention (Speer and Goodrick, 2022).

There are many active branches of wildfire study, each presenting their own persisting challenges. These include (but are not limited to): the combustion of different fuel types (Santoni et al., 2014; Liu et al., 2021; Sullivan, 2022); distribution of fuels in a fuel bed (Catchpole et al., 1989; Khan et al., 2023); investigation of terrain influence on fire spread (Malangone et al., 2011; Ambroz et al., 2019; Hilton and Garg, 2021; Ribeiro et al., 2023); generation and spread of spotfires (Boychuk et al., 2009; Martin and Hillen, 2016; Bonta et al., 2017; Urban et al.,

* Corresponding author.
E-mail address: sam.harris.16@ucl.ac.uk (S.J. Harris).

https://doi.org/10.1016/j.envsoft.2024.106303
Received 12 August 2024; Received in revised form 6 December 2024; Accepted 12 December 2024
Available online 18 December 2024

2019); and the deployment and optimisation of fire management and suppression efforts (Izhaki and Adar, 1997; Hu and Sun, 2007; Ausonio et al., 2021; Yfantidou et al., 2023). The focus of this paper is on the following two topics: the modelling and simulation of wildfire spread (Weber, 1991; Papadopoulos and Pavlidou, 2011; Bakhshaii and Johnson, 2019); and the coupled interaction of the wildfire with the atmosphere (Clark et al., 1996b; Sun et al., 2009; Mandel et al., 2011; Bakhshaii and Johnson, 2019).

1.2. Existing wildfire and wildfire-atmosphere models

Wildfire modelling is of use for all three regimes of pre-, mid- and post-fire analysis. Specifically, wildfire modelling can be used to: model a hypothetical future wildfire and assess the wildfire risk on a given landscape; to predict the future spread of a currently active wildfire; and to reproduce and analyse the spread of a previous wildfire event. A number of wildfire (and general fire) spread models have been developed over the past 80 years and categorised into statistical, empirical and physical models (as in e.g. Weber, 1991) offering increasing levels of physical description. The first fire spread model was that of Fons (1946), a physical model measuring the rate of spread between discrete fuel blocks (or 'particles'). Subsequent physical models were developed (see table 1 of Pastor et al., 2003) with varying preferences for certain heat transfer mechanisms over others. Statistical and empirical (i.e. reduced-order) models were favoured for their simplicity yet accuracy; the most widely-used and successfully model (which is still used today Finney, 1998; Andrews, 2018) is that of Rothermel (1972).

There was still the need to include additional physics, in particular to couple the wildfire spread to the surrounding wind field (Clark et al., 1996a). Dynamic weather conditions such as strong, volatile winds cause equally dynamic and often unpredictable wildfire spread (Viegas et al., 2012; Wheeler et al., 2015; Thomas et al., 2017). Furthermore, the wildfire itself affects the overall wind field: the wildfire generates its own wind source known as the pyrogenic wind (Smith et al., 1975; Beer, 1991; Hilton et al., 2018) and ejects air into the atmosphere via a 'fire plume'. Both the fire plume and the pyrogenic wind perturb the background wind field, which then affects the wildfire spread resulting in a two-way coupling between the fire dynamics and the wind field.

Advances in computational fluid dynamics (CFD) allowed for the creation of such coupled wildfire-atmosphere models. A review of these are given in Papadopoulos and Pavlidou (2011) and Bakhshaii and Johnson (2019) and include the semi-coupled models FIRETEC (Linn et al., 2002) and WFDS (Mell et al., 2007), and the fully coupled models CAWFE (Clark et al., 1996a,b), WRF-FIRE (Mandel et al., 2011) and ForeFire/Meso-NH (Filippi et al., 2011). While able to incorporate complex, coupled wildfire-atmosphere interactions, these three-dimensional CFD models come with a high computation cost, and are largely not able to reproduce wildfire data in real time — see table 1 of Bakhshaii and Johnson (2019). These models are thus well suited to pre- and post-fire research, yet there remains a demand for a simple yet accurate reduced-order wildfire-atmosphere model which runs faster than real time and hence can be used operationally in mid-fire scenarios.

1.3. The pyrogenic potential model of Hilton et al. (2018)

One common simplification is to reduce the fully three-dimensional problem to two-dimensions, and turn the focus to modelling the spread of the wildfire on a two-dimensional surface. This is particularly suitable when modelling surface fires – wildfires with fuel elements under 1.8 m tall (Mell et al., 2007) – which are exclusively considered in this work. Cellular automata (CA) models have been used successfully (Achtemeier, 2012; Quaife and Speer, 2021) yet implementing a finer mesh for improved accuracy can cause a rapid increase in computation time and it is debated whether they are able to reproduce all the physical processes associated with wildfire spread (Finney, 1998; Achtemeier, 2012).

An alternative approach is to develop a continuum model which directly tracks the evolving fire line — the two-dimensional curve separating the burnt and unburnt regions of fuel. Sethian (1985) explored such a model derived from experimental results in Markstein (1951), and Osher and Sethian (1988) subsequently developed a numerical method based on Huygens' principle (see e.g. Finney, 1998) to compute the evolution of the fire line. This was the foundation of the level set method (Sethian, 2001) which has since been used successfully (Mallet et al., 2009; Sharples et al., 2013; Hilton et al., 2016) and is the basis of the SPARK framework (Miller et al., 2015).

This numerical method is also used in another wildfire model which is of particular interest in this work. Over nearly the past decade, a two-dimensional continuum model of surface fire spread incorporating a dynamic, wildfire-atmosphere interaction has been successfully developed in the works of, for example, Hilton et al. (2018), Sharples and Hilton (2020) and Sharples et al. (2022). It is assumed that the wildfire spreads on flat terrain through a single type, homogeneously distributed surface fuel, thus the wildfire evolution is affected by only two factors. The first is a basic rate of spread (ROS) term: some (known) constant capturing the physical, chemical and thermodynamic processes of combustion and heat transfer for a given fuel element. The second is the surrounding wind field: this is in turn composed of some constant, unidirectional ambient wind and the self-induced pyrogenic wind. The pyrogenic wind velocity can be written as the gradient of some pyrogenic potential function ϕ which must be solved for in the region exterior to the fire line, hence this model is referred to as the 'pyrogenic potential model'.

This model has been shown to perform well, demonstrating good agreement between experimental wildfire data on the metre and tens of metres scales, with outputs computed in the order of seconds (Sharples and Hilton, 2020). It can replicate features of wildfire spread that existing two-dimensional models cannot, including the rounding of the fire line into a parabolic shape and the attraction of two disjoint fire lines towards each other. Additional factors can also be incorporated into the model, including terrain (Hilton and Garg, 2021) and vorticity effects (Sharples and Hilton, 2020).

1.4. Main research objectives

The main objective of this work is to develop an alternative, simple, two-dimensional wildfire-atmosphere model which successfully captures the main features of wildfire spread. Following Hilton et al. (2018), these features are: the development of the fire line into a parabolic shape; the closing of the V-shaped wildfires (or junction fires); and the attraction of two wildfires towards each other. The wildfire evolution model is then computed by two efficient and conceptually simple numerical methods which are employed for the first time in the field of wildfire research: a conformal mapping method used to model the spread of a single wildfire; and the AAA-least squares (AAA-LS) algorithm which can model the spread (and merger) of multiple wildfires and spotfires. The wildfire model developed here is thus split into two models: the single wildfire and multiple spotfires models, respective to the numerical method used in computing the wildfire evolution. While the conformal mapping and AAA-LS numerical methods have been applied to a variety of problems, for example in fluid dynamics and electrostatics (Goldstein and Reid, 1978; Trefethen, 2018; Grodzki and Szymczak, 2019; Harris and McDonald, 2023), their use in modelling and predicting wildfire spread appears to be new. Their introduction and implementation into the wildfire problem is thus the main focus of this work.

As outlined in Section 1.2, there is a scarcity of reduced-order, coupled wildfire-atmosphere models capable of running faster than real time which accurately capture the main features of wildfire spread. The numerical methods introduced in this work are able to provide an accurate representation of the wildfire-atmosphere interaction and produce outputs on the order of seconds or minutes. Furthermore, the numerical

methods of this work are immediately capable of incorporating numerous extensions, such as heterogeneous fuelbeds and firebreaks, terrain effects, wildfire merger and fire-related vortices, with no substantial change in the fundamentals of the numerical methods and no significant addition to their runtime. The scope of these numerical methods and their computational speed and conceptual simplicity are their key advantages over existing methods, with this work simply offering an introduction into their use.

The model of this work is inspired by the pyrogenic potential model of Hilton et al. (2018), as detailed in Section 1.3. Both the present numerical model and the pyrogenic potential model treat the surface fire as a two-dimensional free boundary problem and model the exterior, pyrogenic wind flow by a Laplace equation of the pyrogenic potential. Furthermore, both consider a basic ROS, pyrogenic and ambient wind effects, with the upcoming Eq. (7) an exact analogy of Eq. (12) from Hilton et al. (2018). There are, however, three notable differences between the present numerical model and the pyrogenic potential model. First are the numerical methods used, as discussed above. While this work introduces the conformal mapping and AAA-LS methods, Hilton et al. (2018) use the SPARK framework (Miller et al., 2015) to compute the evolution of the fire line, which is based on the level set method (Osher and Sethian, 1988; Mallet et al., 2009). All methods produce comparable results and have comparable runtimes, with the SPARK framework running on the order of seconds (Sharples and Hilton, 2020) and the numerical methods of this work on the order of seconds to minutes. It is not determined which numerical method is superior, nor is that the aim of this work, which is to present alternative, accurate approaches based on the conformal mapping and AAA-LS numerical methods.

Second, there exists a 'fire plume' over the burnt region of the wildfire which ejects air vertically into the atmosphere, essentially driving the flow of the pyrogenic wind. In Hilton et al. (2018), this is modelled by an additional interior Poisson equation with forcing term ν which must be solved for. In this work, the fire plume is simply modelled as an effective sink of strength Q, reducing the problem to the exterior region of the wildfire only to allow the use of the conformal mapping and AAA-LS methods. Third, the basic ROS term in this work is explicitly split into its radiative and convective components. This is a substantial and non-trivial distinction to make: the convective basic ROS term will interact directly with the wind field while the radiative part will not. As will be explored in this work, the exclusion of either term results in two extreme, unphysical scenarios. It should be noted that neither of these scenarios appear in the work of Hilton et al. (2018), suggesting that this distinction is implicitly included in their model as their basic ROS is taken to be a single joint constant u_0. As shown throughout this work and in particular in Section 4.1, both the present numerical model and the pyrogenic potential model produce equivalent results that compare well with experimental data, despite these three key differences. This strengthens the claim of this work that the new models and numerical methods introduced here are practical alternatives to those of Hilton et al. (2018).

This paper is laid out as follows. The mathematical models for both the single wildfire and multiple spotfires problems are introduced in Section 2. The conformal mapping and AAA-LS methods used to numerically solve these problems are then detailed in Section 3. Section 4 presents the numerical outputs from the models. First, the models are validated by comparing their numerical results with those of the pyrogenic potential model from Hilton et al. (2018) and experimental results produced in Sullivan et al. (2019). Second, the wildfire models are then applied to further (theoretical) single and multiple wildfire scenarios, with investigation performed into the effects of the pyrogenic wind and the radiative and convective basic ROS on the fire line development. Third, examples involving firebreaks such as roads, rivers and lakes are also studied. A discussion of the results produced in this work, and a comparison and review of the success of the two new numerical methods, is given in Section 5. Concluding remarks and discussion on future research directions are presented in Section 6.

2. Model setup

A mathematical model for the wildfire problems considered in this work, namely the cases of single wildfire spread and multiple spotfires spread and merger, is given in this section. The effects of terrain (elevation and slopes) and heterogeneous fuel beds on the wildfire spread are not explored in this work. Thus for all problems, it is assumed that all wildfires spread on a flat bed of homogeneously distributed, single-type fuel in the presence of a uniform, unidirectional, constant ambient wind. Surface fires are exclusively considered in this work, i.e. the wildfire(s) spreads through surface fuels such as grasses, heather, fallen leaves and twigs and shrubs less than 1.8 m tall (Mell et al., 2007). This implies that the horizontal length scale of the wildfire(s) is suitably larger than the vertical flame height H and thus all wildfire problems considered here can be treated as two-dimensional.

2.1. Single wildfire model

The single wildfire model is illustrated in Fig. 1. The main feature of interest is the fire line (or fire perimeter) denoted by γ — the finite, closed Jordan curve separating the two distinct regions of singly-connected, finite-area burnt R and unburnt Ω fuels. Modelling the wildfire spread becomes that of finding the evolution of this curve when subject to various dynamical effects. In practice, this amounts to solving for the velocity of the fire line in the normal direction $\hat{\boldsymbol{n}}$ — tangential velocities do not affect the outward spread of the fire. In this work, three key factors are considered which affect the normal velocity v_n.

First, the basic rate of spread (ROS) term v_0 (a velocity with units ms^{-1}) captures the physical, chemical and thermodynamic processes involved in fuel ignition and heat transfer. In the absence of all other external factors such as wind and terrain, the wildfire spreads at this constant speed v_0 in the direction of the local normal to the fire line. The exact value of this ROS term for different fuels is still an open question, see the review articles by e.g. Sullivan (2009) and Morvan et al. (2022), due to a continued lack of understanding of both the ignition process and of the relative magnitudes of convection and radiation in heat transfer. Others have proposed models in which the ROS is calculated deterministically rather than given as an ad-hoc constant (McDonald and Harris, 2024; Dipierro et al., 2024).

In this work, an analysis into neither the value of v_0 nor the quantity $\alpha \in [0, 1]$ representing the (dimensionless) proportion of ROS relating to radiative effects (so that $(1 - \alpha)$ represents the convective effect) is performed here. Instead, the basic ROS is simply taken as some constant $v_0 = \alpha v_0 + (1 - \alpha)v_0$ for a given α. This explicit distinction between radiative and convective terms[1] has been similarly proposed in previous literature. For example, the work of Beer (1991) evaluates the energetics of each distinct heat transfer mechanism in fire spread and a similar dimensionless parameter P representing the ratio of radiative heating by the flame and convective cooling of the fuel bed was introduced in Baines (1990).

Second, there is a unidirectional, constant strength ambient wind $\boldsymbol{u}_a = U_a\hat{\boldsymbol{u}}_a$ present, of magnitude $U_a\mathrm{ms}^{-1}$ and dimensionless, unit direction $\hat{\boldsymbol{u}}_a$. It is assumed that the fire line γ is entirely permeable to this ambient wind, thus all sections of the fire line experience the same (constant) ambient wind effect. The side of the fire line facing the oncoming ambient wind is labelled as the windward side and the opposite side as the leeward side. Third, the fire itself generates a pyrogenic (or fire) wind $\boldsymbol{u}_p$ (units ms^{-1}) (Trelles and Pagni, 1997; Lareau and Clements, 2017; Thomas et al., 2017; Hilton et al., 2018; Sullivan et al., 2019). Air in the burnt region R is ejected vertically out of the two-dimensional system in Fig. 1. The resulting low pressure at the fire line induces a horizontal (dynamic) pressure gradient, driving

[1] It is assumed that conductive effects are sufficiently weak that they can be neglected.

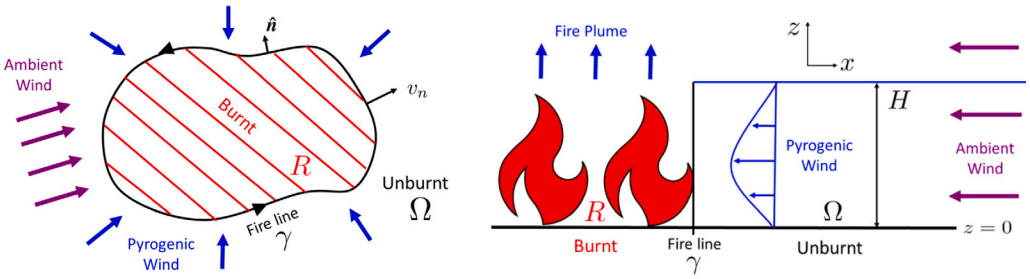

Fig. 1. The single wildfire model from a plan view (left) and side view (right). The blue arrows represent the direction of the pyrogenic (fire) wind and the purple arrows the direction of an ambient wind.

a pyrogenic wind towards the fire line where it too is ejected as part of the fire plume. The overall wind vector can then simply be written as the linear combination of the ambient and pyrogenic winds $\boldsymbol{u} = \boldsymbol{u}_p + \boldsymbol{u}_a$ where all quantities are velocities with units ms^{-1}.

Note that the ROS and ambient wind $\boldsymbol{u}_a$ have purely kinematic effects on the fire line evolution. In contrast, the pyrogenic wind is a dynamical effect since the shape of the fire line determines $\boldsymbol{u}_p$. Thus the co-evolution of $\boldsymbol{u}_p$ and the fire line represents a nonlinear, two-dimensional free boundary problem.

Some simplifying assumptions are made. First, the ambient wind is such that it is not deviated by the fire plume (the permeability assumption mentioned above). Second, any (vertical) deviations of the fire plume induced by the ambient wind do not affect the wildfire spread at the horizontal, surface plane. Third, the fire plume acts as a sink on the surface, drawing in surrounding air. The strength Q (units $\mathrm{m}^2\mathrm{s}^{-1}$) of the fire plume, the effective strength of the sink, is assumed constant for all time. An extension of the model involving a time varying plume strength as the fire grows is of interest and has been explored in previous work — see Harris and McDonald (2022).

While the basic ROS and ambient wind are given constants, the pyrogenic wind must be solved in the fire line exterior Ω for the evolving fire line γ. To good approximation, the pyrogenic wind can be treated as an irrotational flow of an incompressible fluid, thus $\boldsymbol{u}_p = \boldsymbol{\nabla}\phi$ where ϕ is the so-called pyrogenic potential (Hilton et al., 2018; Sharples and Hilton, 2020; Quaife and Speer, 2021; Harris and McDonald, 2022) satisfying the Laplace equation

$$\nabla^2\phi = 0 \quad \text{in } \Omega. \tag{1}$$

The pyrogenic wind is assumed to flow horizontally in a shallow layer of depth H at ground level – the same as the flame height in Fig. 1 – with $\boldsymbol{u}_p$ the average wind velocity over H. Consider its Reynolds number $\mathrm{Re} = UH/D$, where U is some representative speed of the pyrogenic wind and D is its horizontal (momentum) diffusivity. From figure 6 of Bebieva et al. (2020) and table III of Beer (1991) using an ambient wind speed of $U_a = 1\ \mathrm{ms}^{-1}$ (a representative value used throughout this work), it follows that $U = 0.5\ \mathrm{ms}^{-1}$, $H = 0.5$ m and $D = 1\ \mathrm{m}^2\mathrm{s}^{-1}$ and so $\mathrm{Re} \approx 0.25$. Thus the shallow pyrogenic wind flow is of sufficiently low Reynolds number here such that the Navier–Stokes equations reduce to Stokes flow. Integrating across the fluid layer of depth H (see e.g. Gustafsson and Vasil'ev, 2006) it follows that $\boldsymbol{u}_p = \boldsymbol{\nabla}\phi \sim -\boldsymbol{\nabla}p$. Thus the pyrogenic potential ϕ is proportional to the negative pressure $-p$.

Dynamic pressure best describes the cause of pyrogenic wind flow rather than the simple entrainment laws often used in plume dynamics (Smith et al., 1975). The low pressure at the fire line (caused by the fire plume) is modelled by the boundary condition $p = \phi = 0$ on γ without loss of generality. In the far field, the fire plume is observed as an effective sink of strength Q and thus $\phi \to -(Q/2\pi)\log r$ as $r \to \infty$. Note that Hilton et al. (2018) treat the fire plume differently, instead solving an additional Poisson equation in the burnt region R dependent on the upwards air flow $\nu = -w_z$. As shown in Section 4.1, the formulation of the pyrogenic wind used here gives similar quantitative results and matching with experimental data as in Hilton et al. (2018).

Finally, the equation for v_n, the normal velocity of the fire line γ, can be formulated. This has the same form as in Hilton et al. (2018), namely

$$Av_n = v_0 + \tilde{\beta}\hat{\boldsymbol{n}}\cdot\boldsymbol{\nabla}\phi + \tilde{\lambda}\hat{\boldsymbol{n}}\cdot\boldsymbol{u}_a, \tag{2}$$

where $\tilde{\beta}$, $\tilde{\lambda}$ are dimensionless constants and A is a non-dimensional constant found *a posteriori* when comparing the wildfire propagation with experimental data — see Section 4.1. One final modification must be made to Eq. (2) to ensure the fire line satisfies the entropy condition (Sethian, 1985) which states that the fire line cannot intersect previous iterations of itself: once a fuel element is burnt, it cannot become unburnt ie $v_n \geq 0$. The radiative proportion of the basic ROS αv_0 satisfies this automatically. However, the convective effects of the basic ROS $(1-\alpha)v_0$, the pyrogenic wind $\boldsymbol{u}_p$ and the ambient wind $\boldsymbol{u}_a$ may be large and negative, especially on the windward side of the fire. This wind may be sufficiently strong to stop fire spread by convection (not radiation) but not so strong as to push the fire line backwards, which is nonphysical. Therefore, Eq. (2) is modified as

$$Av_n = \alpha v_0 + \max[0, (1-\alpha)v_0 + \tilde{\beta}\hat{\boldsymbol{n}}\cdot\boldsymbol{\nabla}\phi + \tilde{\lambda}\hat{\boldsymbol{n}}\cdot\boldsymbol{u}_a], \tag{3}$$

ensuring that convective (wind) terms have a non-negative effect on the fire line velocity.

2.2. Non-dimensionalisation

Non-dimensional quantities are introduced by scaling with respect to a characteristic velocity and length: the basic ROS velocity v_0 and the initial wildfire radius $R_0 = R(0)$. In particular, R_0 is the conformal radius (Bazant and Crowdy, 2005) in conjunction with the conformal mapping method in Section 3.1. The pyrogenic potential is also scaled by Q, the (constant) strength of the fire plume. The resulting (starred) dimensionless variables are

$$\boldsymbol{x} = R_0\boldsymbol{x}^*, \quad t = \frac{AR_0}{v_0}t^*, \quad \boldsymbol{\nabla} = \frac{1}{R_0}\boldsymbol{\nabla}^*, \quad \phi = \frac{Q}{2\pi}\phi^*. \tag{4}$$

Dropping stars immediately, the normal velocity equation (3) becomes

$$v_n = \alpha + \max[0,\ (1-\alpha) + \beta\hat{\boldsymbol{n}}\cdot\boldsymbol{\nabla}\phi + \lambda\hat{\boldsymbol{n}}\cdot\boldsymbol{u}_a]. \tag{5}$$

where the new dimensionless parameters are

$$\beta = \frac{\tilde{\beta}\left(\frac{Q}{2\pi R_0}\right)}{v_0} = \frac{\tilde{\beta}U_p}{v_0}, \quad \lambda = \frac{\tilde{\lambda}U_a}{v_0}. \tag{6}$$

Note the labelling $U_p = Q/2\pi R_0$: this is the dimensional magnitude of the pyrogenic wind. The full non-dimensional system governing the motion of the fire line γ in the single wildfire problem is thus given by

$$v_n = \alpha + \max[0,\ (1-\alpha) + \beta\hat{\boldsymbol{n}}\cdot\boldsymbol{\nabla}\phi + \lambda\hat{\boldsymbol{n}}\cdot\hat{\boldsymbol{u}}_a] \quad \text{on } \gamma, \tag{7}$$

$$\nabla^2\phi = 0 \quad \text{in } \Omega, \tag{8}$$

$$\phi = 0 \quad \text{on } \gamma, \tag{9}$$

$$\phi \to -\log r \quad \text{as } r \to \infty. \tag{10}$$

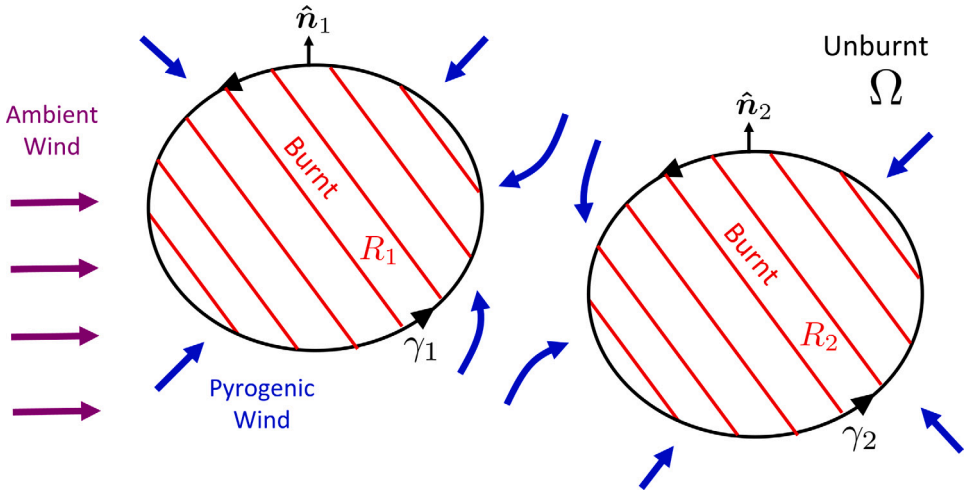

Fig. 2. The multiple spotfires model. The figure shows two wildfires from a plan view. The blue arrows represent the direction of the pyrogenic (fire) wind and the purple arrows the direction of the ambient wind.

Finally, consider the relative magnitudes of the parameters in Eq. (7) by comparing with the values used in Hilton et al. (2018) and observations made in Beer (1991). Wind is the dominant effect and so $\beta, \lambda = \mathcal{O}(10)$, though some $\mathcal{O}(1)$ values may be used in this work for illustrative purposes. By comparing the values of fire and ambient ('mid-flame') winds from Table III of Beer (1991), it is assumed that $\lambda \approx 2\beta$. Similarly from their Table II, comparing convective and non-convective (radiative) heat fluxes in the absence of an ambient wind gives an approximate value of $\alpha \approx 0.5$. Unless stated otherwise, these parameter values will be used throughout this work.

2.3. Multiple spotfires model

The multiple spotfires problem illustrated in Fig. 2 is a simple extension to the single wildfire problem in Section 2.1. Consider a system of multiple wildfires spreading, interacting and perhaps merging with each other. These wildfires may have started independently or be a system of spotfires attributed to one or more main wildfires. While the stochastic generation of spotfires is a topic of interest – see for example Boychuk et al. (2009), Kaur et al. (2016) and Martin and Hillen (2016) – the production of spotfires is not considered in this work. Instead, it is assumed that there are $J \geq 1$ wildfires present initially and that this value J will not increase over time, though it may decrease if two or more wildfires merge.

The total burnt region is now defined as $R = R_1 \cup R_2 \cup \cdots \cup R_J$, where R_j is the burnt region of wildfire j with fire line $\partial R_j = \gamma_j$, and $\Omega = \mathbb{C} \setminus R$ is the unburnt region. The velocity $[v_n]_j$ of fire line γ_j in the direction of its outward unit normal vector $\hat{\boldsymbol{n}}_j$ is of the same form as Eq. (7)

$$[v_n]_j = \alpha + \max[0,\ (1-\alpha) + \beta \hat{\boldsymbol{n}}_j \cdot \nabla\phi + \lambda \hat{\boldsymbol{n}}_j \cdot \hat{\boldsymbol{u}}_a] \quad \text{on } \gamma_j, \tag{11}$$

where the pyrogenic potential ϕ as defined in Section 2.1 satisfies Laplace's equation (8) in Ω and the Dirichlet boundary condition equation (9) at all γ_j. Each wildfire j has a fire plume above its burnt region D_j and it is assumed that these plumes do not interact with each other (nor with the ambient wind as assumed in Section 2.1). Therefore, each wildfire is observed in the far field as a point sink at $z = z_j$, where z_j is the conformal centre of wildfire j. Therefore, the dimensionless system of equations governing the pyrogenic potential ϕ is

$$\nabla^2\phi = 0 \ \text{ in } \Omega, \tag{12}$$

$$\phi = 0 \ \text{ on } \gamma_j, \tag{13}$$

$$\phi \to -\log|\Pi_{j=1}^{J}(z - z_j)| = -\log|h(z)| \ \text{ as } r \to \infty. \tag{14}$$

Eqs. (11)–(14) have been non-dimensionalised using the same scalings from Eq. (4) as in Section 2.2. The characteristic length scale R_0 is now the conformal radius of the largest initial wildfire and the velocity scale is still v_0: the basic ROS of the fuel. Further, it is assumed that each wildfire generates a fire plume of constant strength Q which is used in scaling the pyrogenic potential ϕ. This is a simplification, and an alternative scenario not explored here is that smaller fires may have weaker plumes and thus a smaller effective Q. The starting fires in this work are all of comparable size.

3. Numerical methods

Two numerical methods for solving the wildfire problems described in Section 2 are now presented. The first numerical procedure is based on a conformal mapping method and is used exclusively for the single wildfire problem. The second involves the so-called AAA-LS algorithm which can handle both single wildfire and multiple spotfires scenarios.

3.1. Conformal mapping method

Consider first the single wildfire problem of Section 2.1. The two-dimensional nature of the problem means that it can be formulated in the complex $z = x + iy$ plane which immediately permits the use of methods based on complex analysis. One approach used here involves conformal mapping to describe the wildfire spread. Conformal mapping is the transforming of a two-dimensional domain in the 'physical' plane to a 'canonical' domain in another plane, where the angles between points are conserved under the mapping. By the Riemann mapping theorem (see e.g. Brown and Churchill, 2009), there always exists a conformal map $z = f(\zeta, t)$ from the exterior of the unit disk in, say, the $\zeta-$plane to the exterior of the fire line γ at time t in the physical $z-$plane. The conformal mapping process is show diagrammatically in Fig. 3. The main advantage of conformal mapping in this problem is that Laplace's equation (8) and the Dirichlet boundary condition equation (9) are conformally invariant – they are unchanged in this transformation – and so the pyrogenic potential ϕ can be solved exactly in the exterior to the $\zeta-$disk as

$$\phi(\zeta) = -\log|\zeta|. \tag{15}$$

The fire line velocity equation (7) can then be written in terms of this solution and the conformal map $z = f(\zeta, t)$, reducing the system of Eqs. (7)–(10) in the physical $z-$plane to a single equation of Polubarinova–Galin (PG) type. This is a common technique used in solving similar free boundary problems with conformally invariant governing equations, for example in fluid dynamics and mathematical

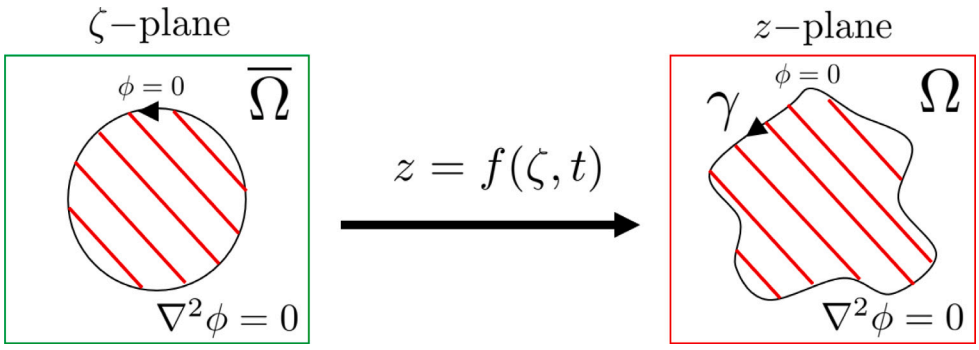

Fig. 3. Pictorial representation of the conformal mapping process. The exterior region $\overline{\Omega}$ of the unit disk in the $\zeta-$plane is transformed to the unburnt region Ω exterior to the fire line γ in the $z-$plane via the conformal map $z = f(\zeta, t)$. The Laplace equation and Dirichlet boundary condition for the pyrogenic potential ϕ are unchanged during this conformal mapping.

biology (Goldstein and Reid, 1978; Entov and Etingof, 1991; Bazant and Crowdy, 2005; Grodzki and Szymczak, 2019; Ladd et al., 2020; Harris and McDonald, 2023).

To formulate the PG equation, note the following relations (Dallaston and McCue, 2013)

$$v_n = \frac{\mathrm{Re}\left(f_t \overline{\zeta f_\zeta}\right)}{|f_\zeta|}, \qquad n = \frac{\zeta f_\zeta}{|f_\zeta|}, \tag{16}$$

where $n = n_x + in_y$ is the complex representation of the outward unit normal vector in the $z-$plane. The pyrogenic wind contribution in Eq. (7) can be written as

$$\hat{\boldsymbol{n}} \cdot \boldsymbol{\nabla}\phi = \frac{\partial \phi}{\partial n} = \mathrm{Re}[n\overline{\nabla}\phi] = 2\mathrm{Re}\left[n\frac{\partial \phi}{\partial z}\right] = -\frac{1}{|f_\zeta|} \quad \text{on } |\zeta| = 1, \tag{17}$$

where $\overline{\nabla} = \partial_x - i\partial_y$. This uses the exact solution of Eq. (15) and the equivalence $|\zeta| = (\zeta\overline{\zeta})^{1/2}$ such that $\partial\phi/\partial\zeta = -1/(2\zeta)$ on the unit $\zeta-$disk $|\zeta| = 1$. Similarly, the ambient wind contribution is

$$\hat{\boldsymbol{n}} \cdot \hat{\boldsymbol{u}}_a = \mathrm{Re}[n\,\overline{u_a}] = \frac{1}{|f_\zeta|}\mathrm{Re}\left[\zeta f_\zeta \overline{u_a}\right] \quad \text{on } |\zeta| = 1, \tag{18}$$

where u_a is the unit ambient wind vector written in complex notation. Thus the PG-type equation is

$$\mathrm{Re}\left(f_t\overline{\zeta f_\zeta}\right) = \alpha|f_\zeta| + \max\left[0,\ (1-\alpha)|f_\zeta| - \beta + \lambda\mathrm{Re}\left(\zeta f_\zeta \overline{u_a}\right)\right]. \tag{19}$$

The numerical task is now to find the conformal map $f(\zeta, t)$ from the unit $\zeta-$disk to the fire line γ. For some special fire line geometries such as circles, ellipses and other n-fold symmetric shapes (Dallaston and McCue, 2016), the map f can be written as the following finite Laurent series,

$$z = f(\zeta, t) = a_{-1}(t)\zeta + \sum_{k=0}^{N} c_k(t)\zeta^{-k}. \tag{20}$$

These are referred to in this work as Laurent shapes where $a_{-1}(0)$ is the initial conformal radius R_0 of the wildfire as defined in Section 2.2. The series is truncated at N terms for numerical purposes; a brief investigation into the effect of increasing the value of N is performed in Section 4.2. This then gives $n = 2N + 3$ unknown real functions in time: $a_{-1}(t)$ and the real and imaginary components of the complex functions $c_k(t) = a_k(t) + ib_k(t)$. Selecting n points around the unit $\zeta-$disk thus converts the PG Eq. (19) into a system of n ODEs in time t for the n unknown functions, which can be solved using any suitable ODE solver; the MATLAB function *ode15i* is used in this work.

For general (non-Laurent) shapes, the approximation equation (20) may be poor for finite N and so the conformal map must be found another way. One approach is to find the map explicitly at each time step, for example by using the SC Toolbox (Driscoll and Trefethen, 2002; Driscoll, 2005). Such an explicit procedure would be computationally expensive and possibly unstable without higher order timestepping procedures, see Section 3.2.

An implicit method can be implemented by combining the approximation equation (20) with a single run of the SC Toolbox to compute the initial conformal map $z = f(\zeta, 0) = g(\zeta)$. The general map $f(\zeta, t)$ can then be written as

$$z = f(\zeta, t) = a_{-1}(t)g(\zeta) + \sum_{k=0}^{N} c_k(t)\zeta^k, \tag{21}$$

with $a_{-1}(0) = 1$ and $c_k(0) = 0$, $\forall k$. The initial conformal radius R_0 of these shapes is now $a_{-1}(0)A$ where A is the conformal radius of the map g. The powers of ζ are of opposite sign to those in Eq. (20) as the SC map $g(\zeta)$ transforms the interior of the unit disk to the exterior of the fire line. When simulating non-Laurent fire line evolution, the PG Eq. (19) is modified to account for the conformal map from interior to exterior; the numerical method is otherwise unchanged from that of Laurent shapes.

3.1.1. Rate of change of area law

An expression for the rate of change of the area $A(t)$ enclosed by the fire line $\gamma(t)$ can be derived, referred to as the rate of change of area (RCA) law. The RCA law can then be used to check the upcoming numerical results. By integrating the velocity v_n over the curve γ and substituting in Eq. (7), the rate of change of area is given by

$$\frac{\mathrm{d}A}{\mathrm{d}t} = \int_\gamma v_n \mathrm{d}s = \alpha\int_\gamma \mathrm{d}s + \int_\gamma \max[0,\ (1-\alpha) + \beta\hat{\boldsymbol{n}}\cdot\boldsymbol{\nabla}\phi + \lambda\hat{\boldsymbol{n}}\cdot\hat{\boldsymbol{u}}_a]\mathrm{d}s. \tag{22}$$

By definition, the first term on the right hand side is the length $L(t)$ of the fire line curve γ. The second term is converted to the $\zeta-$plane by integrating along the unit disk $\zeta = e^{i\theta}$ for $\theta \in [0, 2\pi)$, thus $\mathrm{d}s = |f_\zeta|\mathrm{d}\theta$ where f is the conformal map given by Eq. (20). Using the expressions (17) and (18) gives the RCA law

$$\frac{\mathrm{d}A}{\mathrm{d}t} = \alpha L(t) + \int_0^{2\pi} \max\left[0,\ (1-\alpha)|f_\zeta| - \beta + \lambda\mathrm{Re}\left[\zeta f_\zeta \overline{u_a}\right]\right]\mathrm{d}\theta. \tag{23}$$

3.2. AAA-least squares numerical method

The conformal mapping method from Section 3.1 is difficult to implement in the multiple spotfires scenario as the conformal map from the multiply connected domain to some canonical domain (which is no longer the simple unit disk exterior) cannot be written as a simple Laurent series for all time. Therefore, an alternative method is needed. This would involve explicit timestepping which adds to the computation cost, thus quick methods are sought at each time step to make this procedure more appealing for operational use. There are two processes to consider in constructing this numerical method: how the pyrogenic potential ϕ in the exterior region Ω is calculated at each time step; and how two or more overlapping wildfires are detected and merged into one new wildfire.

3.2.1. Calculating the pyrogenic potential

In the last five years, the AAA-LS algorithm has been created and developed for solving two-dimensional Laplace problems, see the recent review article by Nakatsukasa et al. (2023), and has been applied to a variety of problems in fluid dynamics and electrostatics, see for example (Trefethen, 2018, 2020; Nakatsukasa et al., 2018; Gopal and Trefethen, 2019b; Costa and Trefethen, 2023). The algorithm is based upon the method of fundamental solutions (or the 'charge simulation' method, see e.g. Amano, 1994) and combines the AAA algorithm for finding a rational approximation to some boundary data (Costa, 2020) with a least-squares (LS) fitting procedure, such as in the Lightning Laplace solver (Gopal and Trefethen, 2019b). The algorithm is fast, running in seconds on a standard laptop, and boasts root-exponential convergence with respect to the number of simple poles used (Gopal and Trefethen, 2019b). This method is also designed to handle non-smooth domain boundaries with corner and cusp singularities and can be extended to the domain exterior as well as to multiply connected domains (Trefethen, 2020); all of these extensions are of interest in this work.

The pyrogenic potential ϕ in the unburnt region Ω can be approximated by $\phi = -\log|h(z)| + \mathrm{Re}[F(z)]$, where F is some complex, analytic function in Ω (Trefethen, 2020). The function F can be approximated as

$$F(z) \approx \sum_{j=1}^{J}\left[D_j \log\left(\frac{z-z_j}{z-z_{j'}}\right) + \sum_{n=1}^{N_1} A_{jn}(z-z_j)^{-n} + \sum_{p_{jk}\in D}\frac{B_{jk}}{z-p_{jk}}\right], \quad (24)$$

where $j' = j \pmod J + 1$, z_j is the conformal centre of wildfire j and A_{jn}, B_{jk} are unknown complex coefficients. This approximation consists of three terms. First, a sum of logarithmic terms with unknown real coefficients D_j, where $\sum_{j=1}^{J} D_j = 0$ is implicitly imposed such that there is non-singular behaviour as $z \to \infty$ (Trefethen, 2018; Costa and Trefethen, 2023). Second, a smooth (Runge) polynomial term truncated at N_1. Note that this is a different quantity to the Laurent series truncation N in the conformal mapping numerical method. Third, a singular (Newman) part consisting of simple poles p_{jk} clustered exponentially near corner and cusp singularities in the burnt region i.e. the unphysical region of the problem. While these poles could be placed manually, the AAA algorithm is instead used to generate suitable poles based on the far field function $\log|h(z)|$. Any poles of tiny residue $< \mathcal{O}(10^{-8})$ or that are sufficiently close to the fire line where $\phi = 0$ (at distances less than $\mathcal{O}(10^{-2})$) are then manually excluded to avoid cases of spurious poles or 'Froissart doublets' (Nakatsukasa et al., 2018).

The convergence of the approximation given by Eq. (24) depends upon the number of simple poles produced. In particular, the AAA-LS method offers root-exponential convergence with errors $\mathcal{O}(\exp(-C\sqrt{n}))$, where $C > 0$ is some constant and n are the number of simple poles generated (Gopal and Trefethen, 2019b). Typically in this work, $\mathcal{O}(100)$ poles are produced on each run of the AAA algorithm, and thus it is deemed that the solutions of this work are of suitable accuracy. Therefore, a small value of the power series truncation N_1 can be chosen that still produces convergent results (Trefethen, 2018, 2020). In this work, the value $N_1 = 20$ is chosen throughout, following the representative value used in Costa and Trefethen (2023).

The vector of unknown coefficients $c = [A_{jn}; B_{jk}; D_j]$ is found using an LS algorithm applied to the boundary data z_b, utilising the boundary condition $\mathrm{Re}[F(z_b)] = \log|h(z_b)| = H(z_b)$ on γ_j. Constructing the Vandermonde matrix A of basis vectors (with Arnoldi orthogonalisation included for improved stability — see Brubeck et al., 2021) gives the expression $Ac = H$ and thus c can be found using the backslash operator $c = H\backslash A$. Finally, using the relation $\nabla\phi = \overline{F'(z)}$ from Trefethen (2018), where ∇ is the complex representation of the corresponding vector, it follows that

$$\hat{\boldsymbol{n}}_j \cdot \boldsymbol{\nabla}\phi = \mathrm{Re}[\hat{n}_j \overline{\nabla}\phi] = \mathrm{Re}[\hat{n}_j(-h'(z)/h(z) + F'(z))], \quad (25)$$

which is the pyrogenic wind effect given in Eq. (11). Thus the normal velocity $[v_n]_j$ can be computed for each fire line at a given time step t: the values α, β, λ and $\hat{\boldsymbol{u}}_a$ are known constants and the normal vector $\hat{\boldsymbol{n}}_j$ of each fire line can be computed from the boundary data z_b. A summary of the multiply connected AAA-LS algorithm is given in algorithm 1.

Algorithm 1 Multiply-connected AAA-LS algorithm

1: Input the initial number of wildfires J, fire line boundary data $\gamma_j : z_{jb}$, conformal centres z_j, series truncation N_1 and boundary condition $H = \log|h(z_{jb})|$ on γ_j.
2: Run AAA algorithm to find suitable interior poles p_{jk} for given H. Eliminate Froissart doublets as necessary.
3: Create matrix A of basis vectors $(z_{jb} - z_j)^{-n}$, $1/(z_{jb} - p_{jk})$ and $\log((z_{jb} - z_j)/(z_{jb} - z_{j'}))$. Use Arnoldi orthogonalisation if desired.
4: Run LS algorithm to find unknown vector of coefficients $c = [A_{jn}; B_{jk}; D_j] = H\backslash A$.
5: Form $F(z)$ from equation (24) then $\phi = -\log|h(z)| + \mathrm{Re}[F(z)]$.

The AAA-LS algorithm runs at each time step, with the fire lines then propagated through time using standard Runge–Kutta (RK) methods, see e.g. Butcher (1996). These methods have an accuracy of $\mathcal{O}(\Delta t^n)$ where n is the order of the RK algorithm used, with the AAA-LS method used n times at each time step. In this work, fourth-order Runge–Kutta (RK4) is generally used with an $\mathcal{O}(10^{-2})$ time step. However, the first-order Euler's method (RK1) may be used for simple scenarios (eg circular wildfires) where a similar level of accuracy can be achieved using the same order of time step. The AAA-LS algorithm with RK timestepping offers the speed desired, with an RK1 time step running in around two seconds and RK4 in 8 s on a standard laptop; this is comparable with previous runtimes of the AAA-LS algorithm stated in e.g. Trefethen (2020), Costa and Trefethen (2023).

3.2.2. Detecting and merging two overlapping fire lines

The merging (and splitting) of two free boundaries is a common problem in vortex dynamics (see e.g. Xue et al., 2017) where the boundaries represent the interface between rotational and irrotational flow. The numerical method of contour surgery pioneered by Dritschel (1988) has been successful in enabling complex vortex interaction to be studied. Typically, the numerical problem involves calculating the minimum distance between the two free boundaries and, when this distance falls below some tolerance level, drawing two additional segments to connect the two contours into a single, new closed curve. The MATLAB function *union* used in this work offers a simple approach, with the function correctly ordering and orienting the boundary points of the new merged fire line in the anticlockwise direction. However, the *union* function will only merge the two fire lines if the curves are overlapping and are not just sufficiently close to each other. This is of no consequence to the AAA-LS algorithm which can easily calculate the pyrogenic potential ϕ, even when the fire lines are close together — the pyrogenic potential is very small in the gap region and hence is effectively zero there.

As soon as the fire lines overlap, they are then merged into a single contour. However, the RK4 method will only merge the fire lines (if applicable) at the end of the timestepping procedure. Thus this method will fail if the fire lines overlap during the time step as the AAA-LS algorithm is not designed to handle overlapping contours. Therefore, if a merge occurs during a RK4 step, the code will reset to the beginning of the time step and perform a simple RK1 time step instead. To allow the solution to achieve the same level of accuracy throughout, the RK1 time step will be sufficiently smaller than the one used for the higher order RK method; in this work, an 'emergency' RK1 step size of $\mathcal{O}(10^{-4})$ is typically used. This is another reason why RK1 timestepping may be used instead of RK4: the isochrones of RK4 may not be at equal time intervals between each other if any emergency RK1 steps were used. Therefore RK1 is useful for ensuring that all isochrones are plotted at equal time intervals and thus for comparing isochrones at specific times — this is particularly important in Section 4.1 when comparing the model outputs with experimental data.

Some additional procedures are imposed at each time step over the entire numerical process for added numerical stability. The function *self-intersect* created by Canós (2024) identifies any segments of the fire line which have self-intersected between time steps and removes them from the list of boundary points such that the fire line remains a simple, singly connected curve. Self-intersection is common in the case of extreme junction fires ie V-shaped fires (see e.g. Viegas et al., 2012; Ribeiro et al., 2023) for example those resulting from a fire merger. If the *self-intersect* procedure occurs during an RK4 time step, the time step is aborted and a smaller, emergency RK1 time step is instead performed, as is also employed in the merging procedure. The MATLAB function *smoothdata* smooths any noise in the fire line data without affecting the overall shape of the fire line. Such provisions are necessary for two reasons. First, to allow the user to use a larger time step and still obtain a numerically stable solution; this means the code is computationally quicker and cheaper which is vital for operational use. Second, while the pyrogenic wind is a stabilising effect, the entropy condition in Eq. (11) means that there is no stabilising behaviour on the leeward side of the fire or (often) in the valley between fires. In the single wildfire case, a small magnitude stabilising curvature effect can be used when necessary to impose the stability in these regions. In the multiply connected case, where the explicit computation of curvature could also create numerical errors, the *self-intersect* and *smoothdata* functions are used instead. Finally, the function *interparc* created by D'Errico (2024) interpolates the polygon at each time step to maintain the same resolution of points on the fire line as the wildfire grows.

4. Results

Numerical results for the single wildfire and multiple spotfires models are given here. Outputs are given in the form of isochrones — contours representing the position of the fire line curves at specific times. This section includes a validation of the models of this work when compared against experimental data, before applying the models to further single and multiple wildfire examples, including scenarios with firebreaks in the fuel bed.

4.1. Comparison with results from Hilton et al. (2018)

The single wildfire and multiple spotfires models developed in this work are inspired by the pyrogenic potential model of Hilton et al. (2018), with some notable differences as discussed in Section 1. Thus it is natural to test the accuracy and robustness of the models of this work by reproducing some of the results from Hilton et al. (2018). In particular, their figures 5, 7 and 8 are considered which show the evolution of a line fire and a connected and unconnected junction fire,[2] respectively, all in the presence of an ambient wind flowing in the positive imaginary z direction. The results of the pyrogenic potential model of Hilton et al. (2018) are then compared with experimental fire data performed in the CSIRO Pyrotron — see Sullivan et al. (2019) for the full details of each experiment. The figures and additional data from these experiments, in particular further time steps of figure 8, were kindly provided by the authors of Hilton et al. (2018) and Sullivan et al. (2019) for use in this work.

All three experiments use the same parameters and so the same (equivalent) parameters are to be found and used here. As in Hilton et al. (2018), the basic ROS is $v_0 = 5\times10^{-4}$ ms^{-1} and the ambient wind is of strength $U_a = 1$ ms^{-1} flowing in the positive imaginary z direction. As in Section 2.1, it is taken that $\alpha = 0.5$ and $\lambda = 2\beta = \mathcal{O}(10)$, with the value $\lambda = 20$ found to best match the results. The experiments in figures 5 and 7 of Hilton et al. (2018) run for $t = 15$ s whereas figure 8 runs for $t = 40$ s. It was found that the value $A = 0.24$ gives the best fit to all results, recalling the dimensionless number A from Section 2.1 which scales the time, see Eq. (4). Each line fire has initial length 0.8 m, yet recall from Section 2.2 that the R_0 scaling used here is the conformal radius (of the largest initial fire). The SC Toolbox was used to calculate the initial conformal radii for each experiment, noting that the fire line at dimensional time $t = 5$ s is taken to be the initial fire line here. The scales of the figures are also taken into account when calculating R_0 — figure 5 is displayed on a 1 m ×1 m grid and figures 7 and 8 on a 1.4 m ×0.9 m grid. The initial conformal radii for figures 5, 7 and 8 of Hilton et al. (2018) are $R_0 = 0.25$ m, 0.38 m and 0.24 m, respectively.

The dimensionless final time t_{max} for each experiment can then be calculated using the scaling in Eq. (4): for figures 5, 7 and 8 these are $t_{max} = 1.25, 0.8125$ and 3.52, respectively. Note that the dimensionless scaling in time in (4) depends upon the conformal radius R_0 and so while figures 5 and 7 run for the same dimensional time of 15 s, their dimensionless times are different. For the single wildfire scenarios of figure 5 and 7, the conformal mapping method from Section 3.1 is used. A Laurent series truncation of $N = 128$ is chosen and an $\mathcal{O}(10^{-2})$ curvature effect is included for added stability. For the two wildfire scenario of figure 8, the AAA-LS method is used; RK1 is used with a time step of $t = 4.4\times10^{-3}$ for 800 steps such that isochrones at specific times can be compared with the figures of Hilton et al. (2018) — see Section 3.2.2 for more details.

The purpose of this section is to demonstrate that the conformal mapping and AAA-LS methods can reproduce the main features of the experimental wildfire spread. Therefore, it is acceptable to sacrifice computational speed for improved accuracy. In the conformal mapping method, this is achieved by selecting a higher series truncation value N; an investigation into choosing lower values of N is performed in the upcoming Section 4.2. For the AAA-LS method, an RK1 timestepping method with a very fine time step is used. Finally, all relevant parameters are scaled by a factor 10^{-1}, e.g. $\lambda = 2$ rather than 20, to allow for greater numerical stability. It should again be noted that the same parameters are used for all three experiments here and care has been taken to ensure they match as well as possible with the parameters used in Hilton et al. (2018).

Figs. 4–6 are analogues of figures 5, 7 and 8 from Hilton et al. (2018), respectively, and superimpose the results from the present numerical model (yellow isochrones), the results from the pyrogenic potential model of Hilton et al. (2018) (white isochrones) and the experimental data from Sullivan et al. (2019) (background image) all onto the same plot. In each figure, snapshots of the experimental fire spread are displayed from left to right, top to bottom. Each subfigure is labelled with the dimensional time in seconds (e.g. 5s) since ignition. For the model of this work, the fire line at time 5s is taken to be the initial fire line shape in each case. The white/yellow isochrones displayed are the outputted fire lines of the pyrogenic potential and present numerical models, respectively, at the specified time. The accuracy of the numerical models of this work and Hilton et al. (2018) is then determined by the ability of the computed fire lines to (qualitatively) enclose the burnt region of the experimental fire.

Figs. 4 and 5 show the development of a single line fire and a single connected junction fire, respectively, both of which are perpendicular to the ambient wind. Each scenario had a runtime of around 27 min when using the conformal mapping method, though there was little difference to the $N = 32$ results which ran in 15 s. The model of this work successfully captures the main features of the wildfire development in both experiments: the development of the fire line head into a parabolic shape in the windward direction in Fig. 4 and the closing up of the junction fire in Fig. 5. Furthermore, the fire line shapes qualitatively agree with those from the model of Hilton et al. (2018), though the fire lines differ more noticeably at larger times. However, there is still good agreement between the present numerical model and the experiment; the model still appears to enclose the burnt region of the fire at all times.

[2] This is a V-shaped fire composed of two line fires at an angle θ to each other; the wildfires considered here have $\theta = \pi/2$.

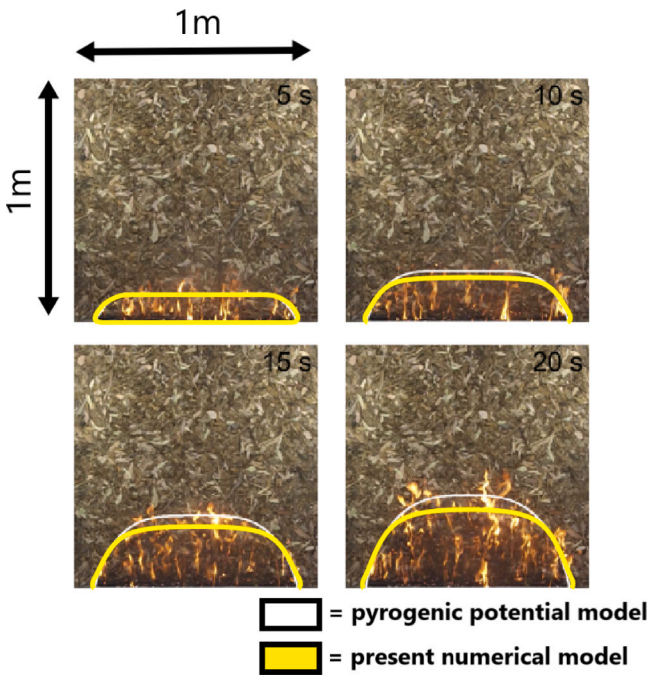

Fig. 4. Propagation of a line fire in an ambient wind: comparison of the single wildfire model with figure 5 of Hilton et al. (2018). Each subfigure shows a snapshot of the experimental wildfire performed in Sullivan et al. (2019) and the predicted wildfire spread from both the present numerical model (yellow line) and the pyrogenic potential model of Hilton et al. (2018) (white line). The experiment is performed on a 1 m×1 m grid and the wildfire spread is displayed at times 5s, 10 s, 15 s and 20 s from ignition (from left to right, top to bottom). The conformal mapping numerical method is used with Laurent series truncation $N = 128$ and runs in 27 min.

Fig. 6 shows the development of an initially disconnected junction fire – two line fires angled towards each other – which had a runtime of around 50 min using the AAA-LS method. There is once again good agreement between the model of this work, the experimental fire and the model of Hilton et al. (2018) over all time. There is some evidence of 'over-rounding' of the fire line: the eastern and western flanks are more curved than in Hilton et al. (2018) and the southern-most points of the wildfire round out also. This is a consequence of the smoothing processes, namely the function *smoothdata* detailed in Section 3.2, applied during the multiple spotfires code to help eliminate numerical instabilities. These small errors are acceptable given that the aim of this work is to produce an operational model capable of capturing the main features of the wildfire spread. Unfortunately, the image of the final fire line at time $t = 45$ s is cut off such that the head of the fire is not visible in the image, nor is there a comparison with the work of Hilton et al. (2018) at this final time step. Nonetheless, it is seen that the model of this work reproduces the burnt region well at this final time step, noting that the two line fires have successfully merged by this time.

To conclude, the present numerical model captures well the main features of the experimental wildfire spread performed in Sullivan et al. (2019) which was also modelled in Hilton et al. (2018). Both the present numerical model and the pyrogenic potential model give qualitatively the same fire behaviour: the development of the leading edge of the line fire into a parabolic head; the closing of the V-shape in the junction fire; and the growth of the two separate line fires towards each other. There are slight differences in the results of each model owing to a number of reasons. While care was made to ensure that the parameters used here match those used in Hilton et al. (2018), the exact parameter values may differ between the models due to the subtle difference in the present model setup, in particular the treatment of the fire plume and the basic ROS. The disparity in outputs may also be due to the difference in numerical methods used and their associated numerical errors. Note also that neither the present numerical model nor the pyrogenic potential model can account for the 3D projection of flames forward of the wildfire and so, even though the fire line successfully encloses the burnt region, there is still evidence of flames extending beyond the fire line. A thorough quantitative comparison between both models and the experimental fires is beyond the scope of this work. Instead, it is concluded, in line with the purpose of this section, that both the present numerical model and the pyrogenic potential model of Hilton et al. (2018) capture well the main features of the wildfire spread and the progression of the fire line.

4.2. Single wildfire results

With validation from Section 4.1 that the present numerical model successfully captures the main features of real world wildfire spread, it is now applied to further theoretical wildfire scenarios. In this section, examples involving a single wildfire are considered and thus the conformal mapping method is used throughout. It is noted here that all further results in this work will involve dimensionless quantities, in line with the non-dimensionalisation procedure in Section 2.2. Therefore, the upcoming length scales of the wildfire – the wildfires considered in this work typically have unit radius – and time scales $t = [t_{min}, t_{max}]$ for which the wildfire spread is computed have no associated dimensional meaning until the user inputs suitable length and velocity scales, R_0 and v_0 respectively. This was done in the previous Section 4.1, where dimensionless quantities were derived from the known dimensional parameters corresponding to the experiments of Sullivan et al. (2019). Further discussion into the significance of the dimensionless results of this work in a dimensional context is given in Section 5.

Consider the simplest case of an initially circular wildfire in a uniform ambient wind of strength $U_a = 1$ in the real z direction. The pyrogenic and ambient wind parameters are $\beta = 10$ and $\lambda = 20$, respectively, and the wildfire evolves for $t = [0, 0.5]$. The circle is a Laurent shape and thus Eq. (20) is a good approximation for the evolving conformal map $z = f(\zeta, t)$, with a series truncation $N = 128$ chosen. Fig. 7 (left) shows the wildfire evolution where six isochrones (the initial fire line and five time steps at equal time intervals) have been plotted. The evolution of the fire line is as expected: the windward side grows solely due to the (radiative) basic ROS whereas growth on the leeward side is amplified in the direction of the ambient wind and rounded into the signature parabolic shape by the pyrogenic wind (Sharples et al., 2022).

The effect of increasing the value of the Laurent series truncation N is also explored, where it is assumed that the higher the value of N, the more accurate the numerical results. The relative error (RE) of the RCA law given by Eq. (23) – see Section 3.1.1 – of the wildfire evolution given in Fig. 7 (left) is computed over time and presented in Fig. 7 (right) with Laurent series truncations $N = 32$, 64 and 128. As expected, this error decreases as the series truncation is increased: the average RE is of $\mathcal{O}(10^{-3})$ for $N = 32$ and of $\mathcal{O}(10^{-5})$ for $N = 128$. The runtime of the code increases for higher N: the runtimes are 7,14 and 117 s for $N = 32, 64$ and 128, respectively. For the purposes of displaying accurate results in this work, the truncation $N = 128$ is used for all future results unless stated otherwise. However, it is noted that the user can sacrifice additional accuracy for computational speed and still obtain numerical results of good accuracy.

Note that the AAA-LS method can also be used to compute single wildfire scenarios. Fig. 8 shows a comparison of the outputs of both the conformal mapping (crosses) and AAA-LS (circles) methods in the case of an initially circular wildfire in a uniform ambient wind of strength $U_a = 1$ in the real z direction. Here, the parameters $\beta = 1.5$ and $\lambda = 3$ are used and $t = [0, 0.5]$. The conformal mapping method uses $N = 128$ and the AAA-LS method uses RK1 timestepping with a time step $t = 0.05$. It is seen that both methods produce similar outputs, with the six isochrones all lying atop each other. The AAA-LS method

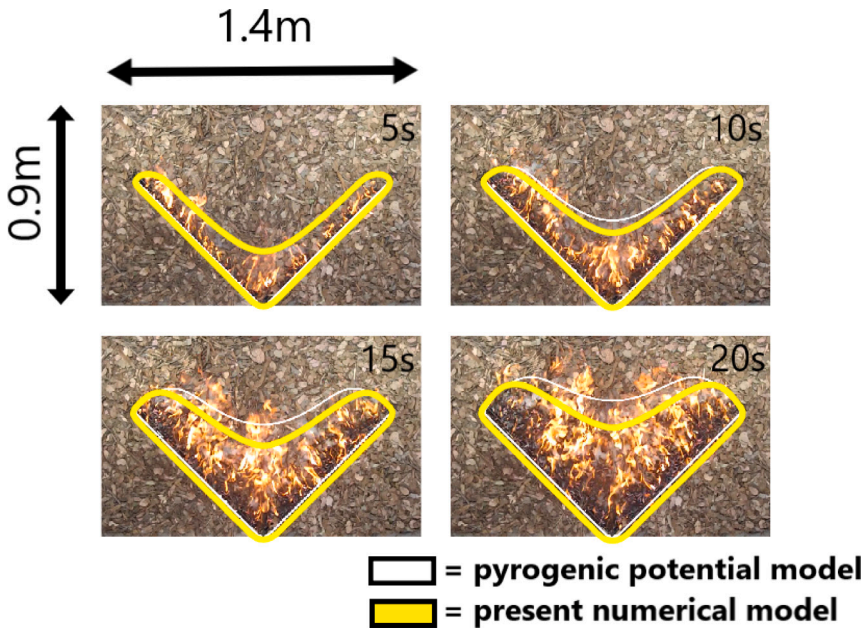

Fig. 5. Evolution of a connected junction fire: comparison of the single wildfire model of this work with figure 7 of Hilton et al. (2018). Each subfigure shows a snapshot of the experimental wildfire performed in Sullivan et al. (2019) and the predicted wildfire spread from both the present numerical model (yellow line) and the pyrogenic potential model of Hilton et al. (2018) (white line). The experiment is performed on a 1.4 m × 0.9 m grid and the wildfire spread is displayed at times 5s, 10 s, 15 s and 20 s from ignition (from left to right, top to bottom). The conformal mapping numerical method is used with Laurent series truncation $N = 128$ and runs in 27 min.

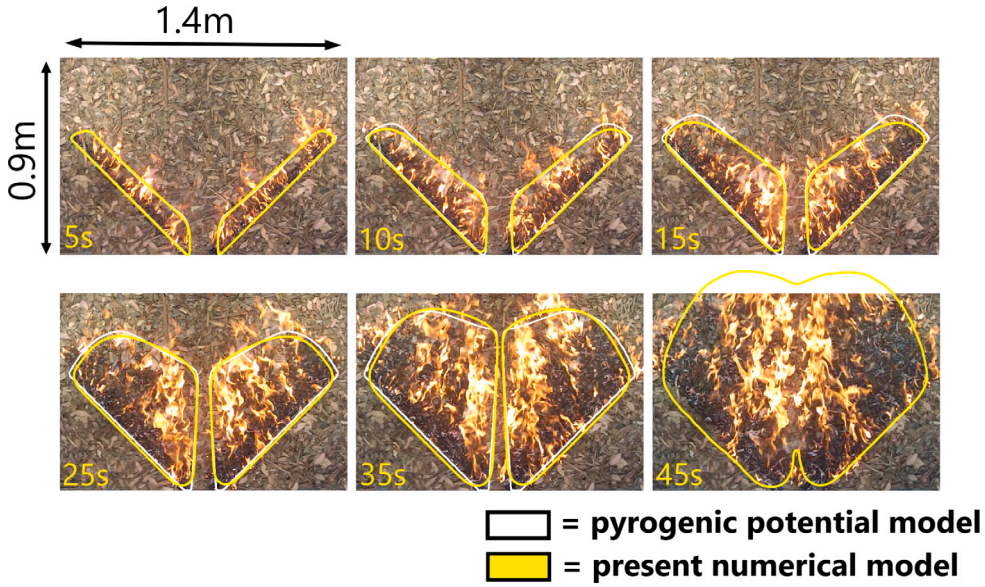

Fig. 6. Evolution of an unconnected junction fire: comparison of the multiple spotfires model with figure 8 of Hilton et al. (2018). Each subfigure shows a snapshot of the experimental wildfire performed in Sullivan et al. (2019) and the predicted wildfire spread from both the present numerical model (yellow line) and the pyrogenic potential model of Hilton et al. (2018) (white line). The experiment is performed on a 1.4 m × 0.9 m grid and the wildfire spread is displayed at times 5s, 10 s, 15 s, 25 s, 35 s and 45 s from ignition (from left to right, top to bottom). The AAA-LS numerical method is used and runs in 50 min.

produces results in 66 s compared to the 45 s runtime of the conformal mapping method.

Following Hilton et al. (2018) – see their Fig. 3 – the effect of the pyrogenic wind on the fire line propagation is investigated. Consider a straight line fire perpendicular to an ambient wind flowing in the imaginary z direction. The initial line fire is approximated by a thin ellipse with conformal map of the form of Eq. (20) where $a_{-1}(0) = 1$, $c_1(0) = 0.9$ and $c_k(0) = 0$ for all remaining $k \in [0, 128]$. The fire line evolves for $t = [0, 0.5]$ for a constant ambient wind parameter $\lambda = 10$ and varying pyrogenic wind effects $\beta = 0.05, 5$ and 10. The isochrones of these three experiments are given in Fig. 9. In agreement with the results of Hilton et al. (2018), it is found that a stronger pyrogenic wind effect causes an increased rounding of the leeward fire line edge into a more pronounced parabolic shape. Additionally, the fire line head does not propagate as far under stronger pyrogenic winds.

Fig. 10 shows the evolution of a variety of initial Laurent and non-Laurent fire line shapes under the influence of different ambient wind directions and wildfire parameter values — these are given in the figure caption. The top row of Fig. 10 shows two Laurent shapes: an irregular pentagon and an hourglass, respectively. These shapes and their initial Laurent coefficients come from Rycroft and Bazant (2016), see their figures 5a and 7a, respectively. The bottom row of Fig. 10 shows the evolution of initial non-Laurent fire line shapes: a bean and a blade, respectively. These come from the work (Gopal and Trefethen, 2019a),

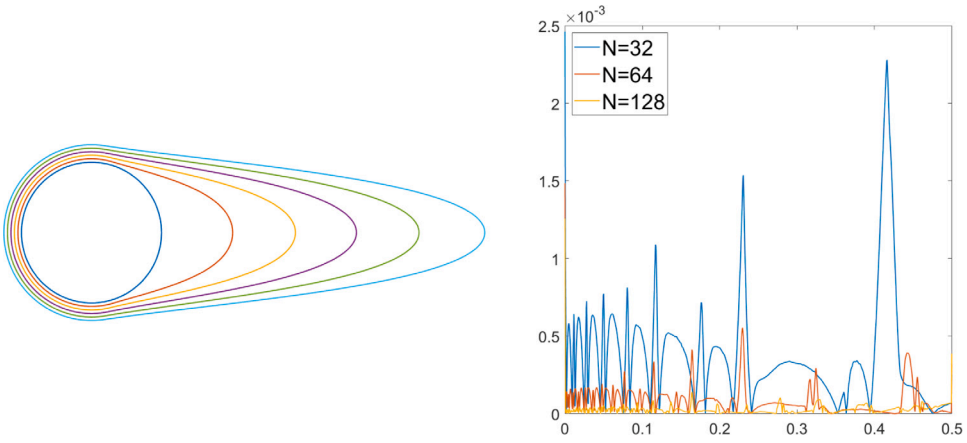

Fig. 7. Evolution of an initially circular wildfire between $t = [0, 0.5]$ in a uniform ambient wind of unit strength in the positive real z direction. The pyrogenic and ambient wind parameters are $\beta = 10$ and $\lambda = 20$ and the Laurent series truncation is $N = 128$. (Left) Six isochrones of the wildfire spread are plotted at equal time increments. (Right) Relative error of the RCA law of the wildfire spread with Laurent series truncations $N = 32, 64$ and 128.

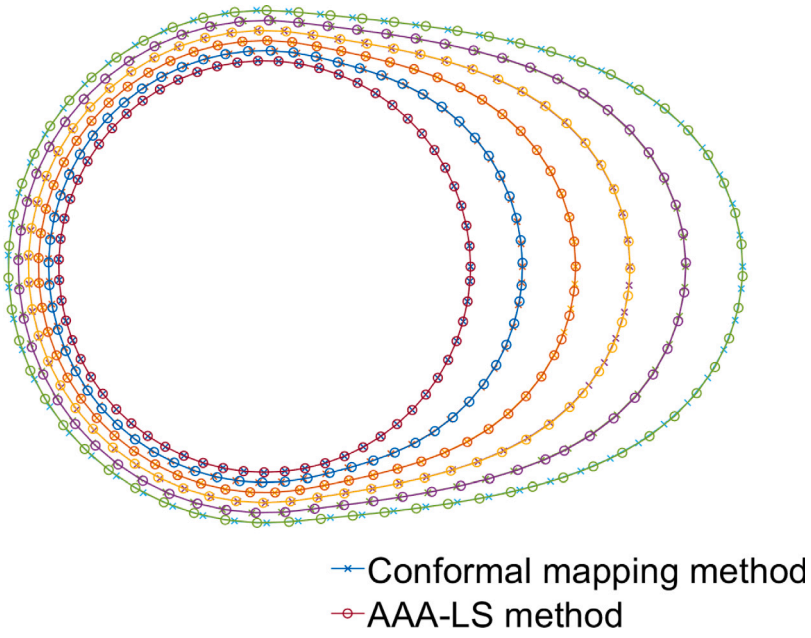

Fig. 8. Comparing the conformal mapping (crosses) and AAA-LS (circles) methods in computing the evolution of an initially circular wildfire evolving in the presence of a uniform ambient wind of strength $U_a = 1$ in the real z direction. Six isochrones are plotted in the time interval $t = [0, 0.5]$ and the values $\beta = 1.5$ and $\lambda = 3$ are used. The conformal mapping method uses $N = 128$ and the AAA-LS method uses RK1 timestepping with time step $t = 0.05$.

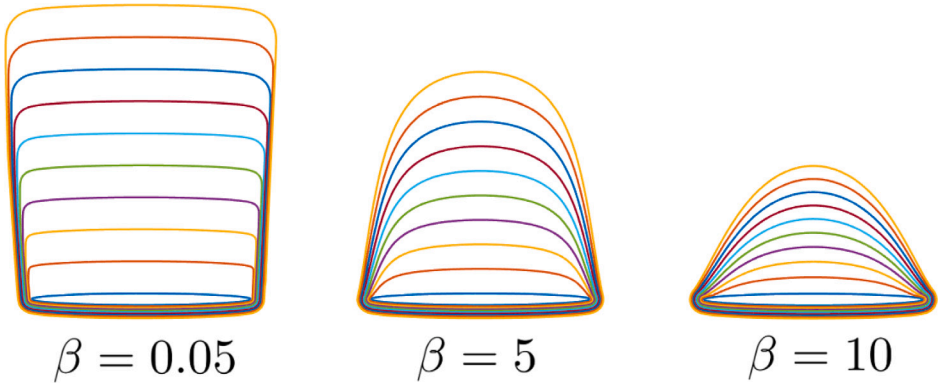

Fig. 9. Evaluating the effect of pyrogenic wind. Three line fires (approximated by thin ellipses) spread in the presence of a uniform, unit strength ambient wind flowing in the positive imaginary z direction. The ambient and pyrogenic wind parameters are $\lambda = 10$ and $\beta = 0.05$ (left), $\beta = 5$ (centre) and $\beta = 10$ (right) and the wildfires evolve for $t = [0, 0.5]$. In each figure, ten isochrones at equal time increments are plotted.

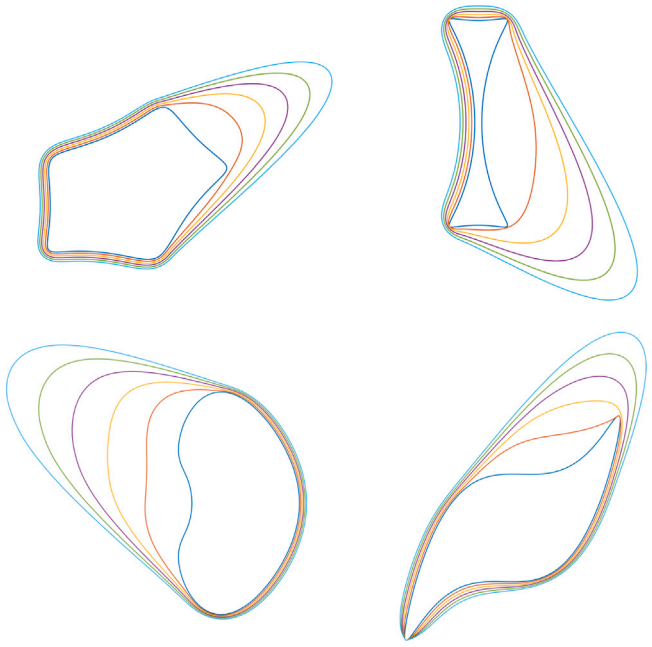

Fig. 10. Fire line evolution of Laurent (top row) and non-Laurent (bottom row) shapes under a constant ambient wind of strength $U = 1$ at angle θ to the horizontal (real axis). Laurent shapes: (Left) irregular pentagonal fire, $\beta = 10$, $\lambda = 20$, $\theta = \pi/6$, $t = [0, 0.25]$. (Right) hourglass fire, $\beta = 18$, $\lambda = 25$, $\theta = -\pi/4$, $t = [0, 0.4]$. Non-Laurent shapes: (Left) bean fire, $\beta = 10$, $\lambda = 20$, $\theta = 5\pi/6$, $t = [0, 0.2]$. (Right) blade fire, $\beta = 6$, $\lambda = 15$, $\theta = \pi/3$, $t = [0, 0.2]$.

see their Fig. 10. Each experiment uses a series truncation $N = 128$ with runtimes in the range of 5 min (pentagon and bean) to 35 min (blade) on a standard laptop. If the user desires, a smaller series truncation $N = 32$ can alternatively be used to obtain quicker runtimes (on the order of seconds) while still providing a solution of good accuracy — as demonstrated in Fig. 7.

In producing the results of Fig. 10, a small effect on the fire line normal velocity proportional to the curvature of the fire line was imposed for added numerical stability. Its magnitude was of $\mathcal{O}(10^{-2})$ for Laurent shapes and $\mathcal{O}(10^{-1})$ for non-Laurent shapes; these were of sufficiently lower order compared to the basic ROS ($\mathcal{O}(1)$) and wind effects ($\mathcal{O}(10)$ such that the main features of the wildfire evolution were unchanged. The curvature effect is especially important on the windward side of the fire line where there is (generally) no pyrogenic wind contribution which also has a stabilising effect. There may be some numerical instabilities due to the crowding phenomenon which is a known challenge in numerical conformal mapping procedures, see e.g. Driscoll (2005). While the n points selected in the $\zeta-$plane are spaced equally around the unit disk, they may not be equally spaced in the physical plane when transformed onto the fire line. This can result in a lack of resolution at some points of the fire line, such as in deep 'troughs'. The curvature effect helps to smooth out any of these instabilities in the numerical method.

4.3. Two and three wildfire results

Next, examples involving multiple wildfires spreading and interacting with each other are considered using the AAA-LS method. Fig. 11 gives the simplest multiple wildfires example of two growing circular wildfires, interacting with each other before merging occurs. Six independent scenarios are presented. The bottom and top rows of Fig. 11 show the growth of the wildfires with and without a unit strength vertical ambient wind present, respectively. The three columns from left to right show the effect of increasing the value of α – the ratio of radiative to convective basic ROS – from 0 (fully convective) to 0.5 (the representative value taken throughout this work) to 1 (fully radiative). In each figure, the values $\beta = 1.5$ and $\lambda = 3$ are selected for illustrative purposes. Furthermore, the wildfires evolve in the time $[0, 0.25]$ with isochrones plotted at intervals $t = 0.05$, with RK1 timestepping used to allow for more direct comparison between the fire scenarios at specific time increments. Each result was created in under four minutes of runtime.

The subfigures of Fig. 11 show distinctive behaviour. Considering $U = 0$, the example $\alpha = 0$ shows wildfire growth only in the region between the two wildfires — the incoming pyrogenic wind is sufficiently strong enough on the remaining sections of each fire line to stop wildfire spread entirely, so that the most pronounced effect is the wildfires growing towards each other. The other extreme $\alpha = 1$ shows the two wildfires growing entirely independently of each other, with the pyrogenic wind effect completely ignored at all points on the fire line due to the entropy condition. However, this is inconsistent with the observations and conclusions drawn in Hilton et al. (2018) which state that two wildfires will interact and grow towards each other (even in the absence of ambient wind). Careful consideration has consequently been taken in this work to separate radiative and convective basic ROS effects in the wildfire model as neglecting either effect results in two (unphysical) extreme cases. The example where $\alpha = 0.5$ gives a good balance between these two extremes: the wildfires grow towards each other but convective effects are not strong enough to entirely stop wildfire spread on non-facing segments of the fire line. The examples with ambient wind $U = 1$ in the imaginary z direction show much the same effects, now with the added rounding of the fire head on the leeward side. Additionally, there is evidence even in the $\alpha = 1$ case that the wildfires grow towards each other. However, this is only seen at the fire head; there is no apparent interaction (as mathematically expected) in the region between the wildfires. Once more, this is inconsistent with theoretical work and experimental observations.

Fig. 12 (top row) shows the growth and eventual merger of three circular wildfires in the absence of ambient wind. The parameter $\beta = 20$ is used and RK4 timestepping is employed, with time steps $t = 0.02$ for each RK4 step and $t = 5 \times 10^{-4}$ for any emergency RK1 time steps. A total of 100 steps are performed with 11 of these steps plotted in Fig. 12; note that these isochrones are now not necessarily at equal time intervals due to the use of RK1 at times of merger and numerical instability. The bottom row of Fig. 12 displays the first (left) and second (right) merger steps, and all results were produced in 28 min of runtime. The resulting wildfire growth is as expected: the wildfires grow more strongly towards each other the closer they get and the concave regions of the fire line following a merger are quickly smoothed out, with both of these effects attributed to the pyrogenic wind. Furthermore, the overall wildfire evolution looks smooth, with any numerical instabilities successfully smoothed out while not changing the main features of the wildfire spread. This is observed between the second and third isochrones after the second merger: the temporary instabilities in the fire junction are smoothed away.

4.4. Firebreaks

The numerical method of this work is also able to model the effects of firebreaks, or more generally segments of the fuel bed which are unable to burn, for example roads, rivers, lakes or areas of previous controlled burning. It is assumed that the firebreaks are sufficiently flat so that both ambient and pyrogenic winds are unaffected by their presence. The positioning of such firebreaks may result in the evolution of fire lines with sharp corners, see for example the upcoming Fig. 14 (left) where the fire line develops corners at it spreads through a rectangular gap. As the AAA-LS method is well equipped to handle such corner and cusp singularities (Costa and Trefethen, 2023) and can compute the evolution of a single or multiple wildfires, the AAA-LS method is used exclusively in this section.

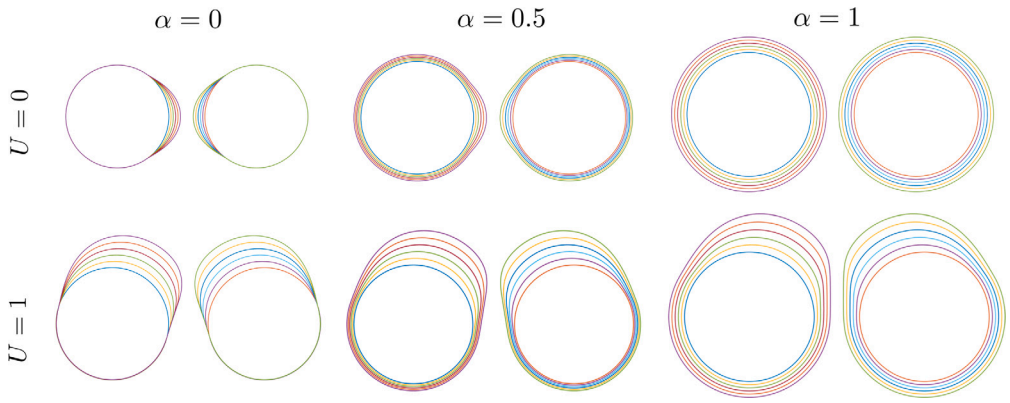

Fig. 11. Six independent subfigures showing the growth of two circular wildfires with (bottom row) and without (top row) a unit strength ambient wind in the positive imaginary z direction for the values $\alpha = 0$ (left), $\alpha = 0.5$ (centre) and $\alpha = 1$ (right). Each fire grows with $\beta = 1.5$ and $\lambda = 3$ for $t = [0, 0.25]$, with isochrones plotted at $t = 0.05$ increments.

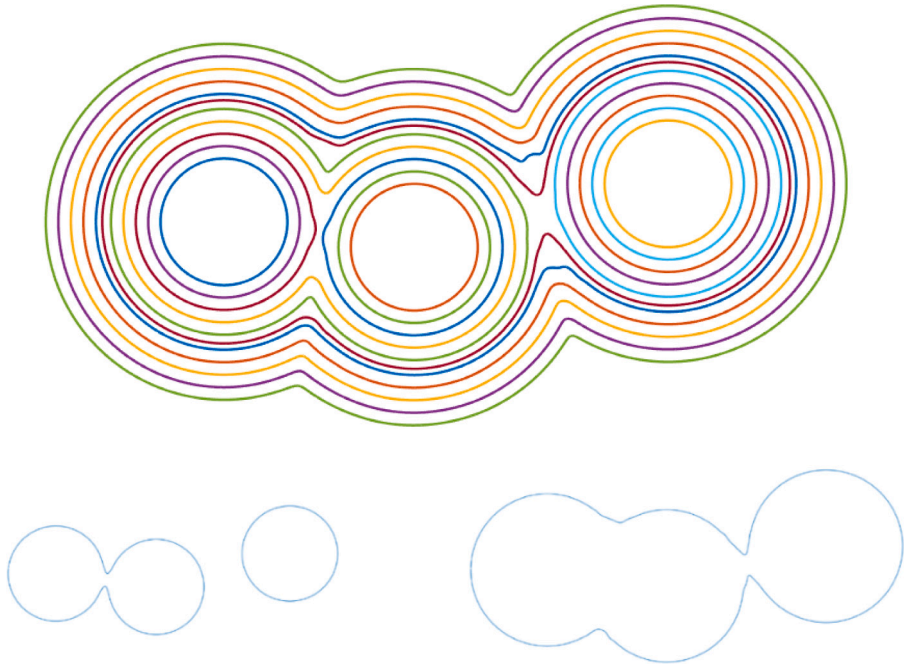

Fig. 12. The spread and merger of three circular wildfires in the absence of ambient wind with pyrogenic wind effect $\beta = 20$ and RK4 timestepping with time steps $t = 0.02$. Of the 100 isochrones calculated, 11 are plotted in (top), with the contours of the first (bottom left) and second (bottom right) mergers identified.

Consider the generalised multiple spotfires scenario of J wildfires with burnt regions R_j and fire lines γ_j, respectively, with the unburnt region defined as $\Omega = \mathbb{C} \setminus [R_1 \cup R_2 \cup \cdots \cup R_J]$. Initially and therefore for all time, there is a (perhaps disconnected) region I consisting of incombustible fuel which is a subset of the unburnt region Ω. A very simple addition is made to the normal velocity equation (11) on each fire line γ_j as follows

$$[v_n]_j = \tau(z)\Big[\alpha + \max[0,\ (1-\alpha) + \beta \hat{\boldsymbol{n}}_j \cdot \boldsymbol{\nabla}\phi + \lambda \hat{\boldsymbol{n}}_j \cdot \hat{\boldsymbol{u}}_a]\Big], \quad \tau(z) = \begin{cases} 0, & z \in I \\ 1, & z \notin I. \end{cases} \tag{26}$$

Although not considered here, inhomogeneous fuel beds could also be described using a similar equation, where sections of the fuel bed speed up or slow down wildfire spread rather than stop it altogether. In such a scenario, consideration must be made whether this would affect the entire normal velocity or simply the basic ROS contributions. The modified normal velocity equation (26) is implemented into the multiple spotfires model and various scenarios considered — there is zero ambient wind in each scenario but pyrogenic wind is still present.

Fig. 13 shows an example involving three initially circular wildfires on either side of a straight road which is modelled by an infinite strip parallel to the imaginary axis. The motivation for this example is that the two fires on the right of the road are smaller spotfires produced from the main wildfire on the left. As stated in Section 2.3, the generation of these spotfires is not discussed in this work. Seven of the 73 isochrones calculated are plotted, where RK1 with a time step of $t = 0.05$ is used. The three initial wildfires are plotted in black, then the isochrones of each fire line are plotted in the same colour for a specific time instance. The parameters $\beta = 10$ and $\alpha = 0.25$ are used for illustrative purposes and the code runs in 770 s. None of the three wildfires penetrate into the road and thus the numerical method successfully accounts for the firebreak. Furthermore, the three wildfires continue to grow towards each other due to the pyrogenic wind — note the lower value of $\alpha = 0.25$ is taken here to emphasise this effect. The two spotfires grow towards the main fire and each other and eventually merge, as visible at the final (purple) isochrone.

Two further firebreak examples involving only a single, initially circular wildfire are given in Fig. 14. The first (left) shows the previous infinite strip scenario with an opening in the middle; this could represent a gap between two purpose-built firebreaks designed to slow the

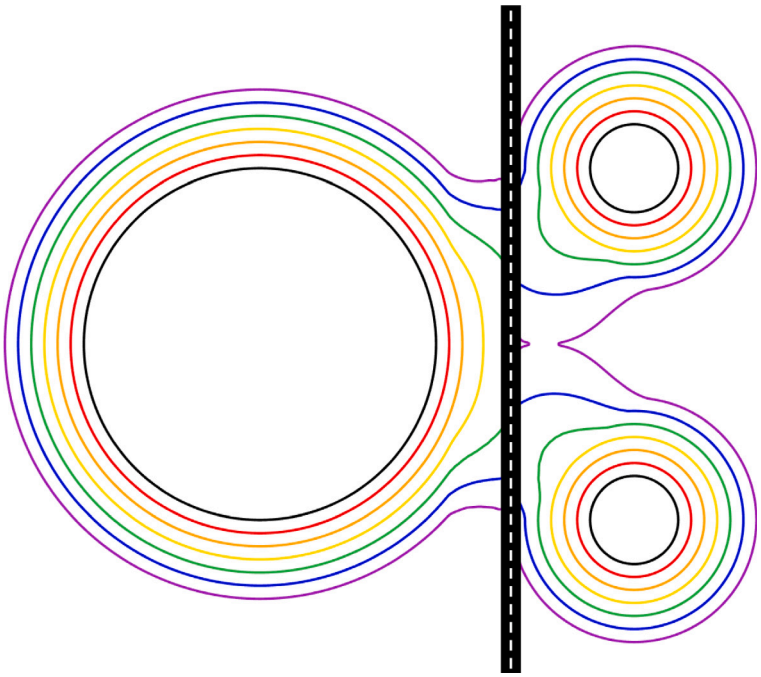

Fig. 13. Three fires spreading in the absence of an ambient wind on either side of a straight road — the infinite strip. The parameters used are $\beta = 10$, $\alpha = 0.25$ and RK1 timestepping with 73 steps of $t = 0.05$: seven of these are plotted showing the wildfire spread at equal time increments. The three initial fire lines are plotted in black, then each fire line is plotted in the same colour at a specific time interval.

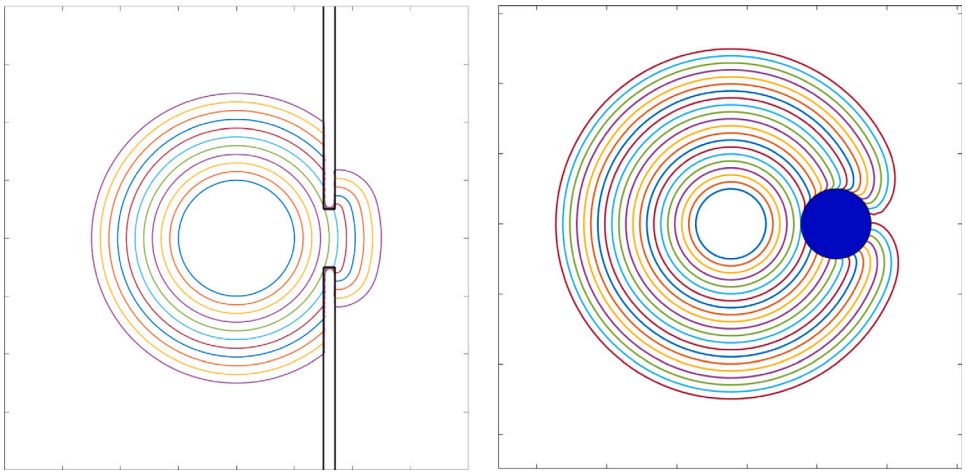

Fig. 14. Evolution of an initially circular wildfire of unit radius in the presence of various fire breaks and in the absence of an ambient wind. Isochrones of the wildfire evolution (coloured lines) are plotted in each figure. Left: a gap in the firebreak — the infinite strip between the black lines. Parameters used are $\beta = 20$ and RK1 timestepping with 30 steps of $t = 0.1$: 11 isochrones are plotted. Right: a circular lake of radius 0.5 — the filled, blue circle. Parameters used are $\beta = 10$ and RK4 timestepping with 40 steps of $t = 0.1$: 21 isochrones are plotted.

wildfire spread rather than stop it altogether. The parameter $\beta = 20$ is taken and RK1 is used with time step $t = 0.1$ for 30 steps, running in a time of 122 s. The wildfire successfully penetrates through the gap in the firebreak, yet the radius of the wildfire spread on the right side is largely reduced from that on the left, as expected. Fig. 14 also shows (right) the spread of a circular wildfire with $\beta = 10$ around a circular lake — the filled, blue circle of radius 0.5 (recall that the length scale is dimensionless following the non-dimensionalisation of the problem in Section 2.2). Here, RK4 is used with time step $t = 0.1$ for 40 steps, running in a time of 570 s. The wildfire splits into two arms which grow around the lake and towards the other arm, with the simulation stopped before the two arms merge. The multiple spotfires model developed in this work cannot account for this type of merger as it would result in two disconnected 'exterior' domains, yet such an extension to the AAA-LS algorithm is possible; this is discussed in Section 6.

5. Discussion

The aim of this work was to create an alternative two-dimensional wildfire-atmosphere model able to capture the main features of wildfire spread. The present numerical model was inspired by the work of Hilton et al. (2018), with Eq. (7) an exact analogy of their Eq. (12). In addition to using an alternative model for the fire plume dynamics and imposing an explicit distinction between convective and radiative basic ROS, the model is different to the pyrogenic potential model in that it introduces two alternative, conceptually simple numerical methods to compute the evolution of the fire line. These are the conformal mapping and AAA-LS numerical methods, which each offer different benefits.

While the conformal mapping method is restricted to computing the evolution of a single wildfire, it is simple and fast even for a large number of time steps and fundamentally consists only of a basic,

implicit ODE solver. The AAA-LS method is more sophisticated yet still conceptually simple and fast, requiring the *chebfun* package (see e.g. Costa and Trefethen, 2023) to couple the AAA algorithm to a standard least-squares fitting procedure. It also requires an explicit RK timestepping routine which adds to the computation speed and introduces associated numerical errors. However, the AAA-LS method can model both single and multiple wildfire spread and is easily adaptable to the case of wildfire merger. Furthermore, the algorithm can handle sharp fire line geometries involving corners and cusps, for example the V-shaped junction immediately following a wildfire merger. The conformal mapping method is less equipped to handle such geometries due to the crowding phenomenon, see e.g. Driscoll (2005). As both methods offer different advantages and disadvantages, both are introduced in this work and assigned to their respective problems: the conformal mapping method is used in the single wildfire model and the AAA-LS method in the multiple spotfires model.

To demonstrate the efficacy of these new numerical models, their outputs are compared against those from the pyrogenic potential model of Hilton et al. (2018) and the experimental results of Sullivan et al. (2019) in Section 4.1. It is found that both models perform well in representing the main features of wildfire spread: the parabolic rounding of the fire line head; the closing of the V-gap; and the growth of multiple wildfires towards each other. Furthermore, both models have comparable computational speed on a standard laptop, with the pyrogenic potential model running in the order of seconds (Hilton et al., 2018; Sharples and Hilton, 2020) and the models of this work on the order of seconds to minutes, depending on the desired accuracy of the output. There are subtle differences in the exact fire line evolution outputted by each model; this is likely due to a disparity in actual parameter values resulting from the differences in each model setup and due to a difference in numerical errors offered by the level set and conformal mapping/AAA-LS methods. It is difficult to identify the burnt region from the experimental images due to the inclined flames (a similar conclusion was reached in Hilton et al., 2018) and thus it cannot be determined which model most accurately computes the wildfire evolution. Instead, it is concluded that both models are of comparable accuracy and thus the model of this work has successfully reproduced the results from Hilton et al. (2018).

The simplicity of the models developed in this work allows for extensions to the wildfire problem to be easily incorporated while not drastically changing the fundamentals of the conformal mapping and AAA-LS methods used. Two extensions were considered here: the merging of two wildfires and the effect of firebreaks (such as roads and lakes) on wildfire spread. To the authors' knowledge, the latter extension has not been applied to the pyrogenic potential model of Hilton et al. (2018), though it would be equally straightforward to do so. Similarly, there are possible extensions to the present numerical model that have been successfully applied to the pyrogenic potential model, including vortex and terrain effects (Sharples and Hilton, 2020; Hilton and Garg, 2021) — these are discussed further in Section 6.

The effects of the two parameters, the ratio α of the radiative to convective basic ROS effects and the strength β of the pyrogenic wind effect, have also been studied in this work. In agreement with Hilton et al. (2018), a higher β value causes a stronger rounding of the fire head that progresses at a slower rate. Increasing α decreases the ability of two wildfires to grow towards each other which, in the case of zero ambient wind, results in the two extreme limits: $\alpha = 0$ where wildfire growth is completely halted on the non-facing portions of the fire line and $\alpha = 1$ where there is no interaction between the two wildfires at all. Interestingly, the pyrogenic potential model of Hilton et al. (2018) does not produce either of these extreme limits, despite making no explicit distinction between radiative and convective basic ROS — their Eq. (12) implies they consider only radiative basic ROS. It is assumed that the additional differences in their modelling assumptions, for example their treatment of the fire plume, implicitly prevents the two unphysical extreme cases.

It is worth highlighting that the results produced throughout this work (excluding those in Section 4.1) are entirely non-dimensional. Thus the features of the coupled wildfire-atmosphere model developed here, in particular the effect of the pyrogenic wind, can be modelled across length scales. The work of Hilton et al. (2018) conclude this also: not only do they validate their model against the metre-scale laboratory experiments of Sullivan et al. (2019), they also show good accuracy when compared to field experiments with initial fire lines on the order of tens of metres — see their Figs. 10 and 11. Thus the model of this work is very practical: the user can use the numerical methods to produce dimensionless results, then apply suitable dimensions as appropriate for a given wildfire on the metre to tens of metres scale.

It is speculated whether the present numerical model is applicable in the case of kilometre scale wildfires also. While no such analysis is performed in Hilton et al. (2018), other wildfire-atmosphere models such as WRF-Fire (Mandel et al., 2011) and ForeFire/Meso-NH (Filippi et al., 2011) can scale from the tens of metres to kilometre scales — see table 1 of Bakhshaii and Johnson (2019). It must be cautioned that wildfires of such large scales may introduce more complex atmospheric coupling not currently considered in the present numerical model. One such example is the dynamics of the fire plume — it is expected that a kilometre scale wildfire would have a substantial fire plume which would significantly interact with the background ambient wind field; such an interaction is neglected in the model of this work. Such an analysis into the added complexities when considering kilometre scale wildfires is beyond the scope of this work.

Finally, it is concluded that the present numerical model can perform on the order of seconds to minutes. When comparing between the experimental results of Sullivan et al. (2019) in Section 4.1, some amount of computational speed was sacrificed to obtain results of improved accuracy, to allow the best possible comparison with the model of Hilton et al. (2018). Various procedures, such as decreasing the Laurent series truncation in the conformal mapping method or using higher order RK timestepping with larger timesteps in the AAA-LS method, can be used to reduce the runtime further. All other results in this work are non-dimensional, thus comparing the runtime of the code with the physical time of the wildfire spread is not possible until suitable dimensions are added. Some representative dimensions are considered for the example of two circular wildfires growing towards each other in Fig. 11. The final dimensionless time is $t^* = 0.25$ and it is assumed that the values $A = 0.24$ and $v_0 = 5 \times 10^{-4}$ as used in Section 4.1 are also applicable in this wildfire problem. Thus the final dimensional time in minutes of the wildfire spread is $t = 20R_0$, where R_0 is the initial dimensional radius of the wildfire. On the metre scale, assuming $R_0 = 1$ m gives that $t = 20$ min and on the tens of metres scale with $R_0 = 10$ m gives that $t = 200$ min $= 3$ hours and 20 min. The runtime of the numerical method is under four minutes which is substantially faster than real time and it is observed that the larger the scale of the wildfire, the quicker the numerical model in comparison to the associated real time scale. Should the present numerical model be applicable to wildfires on the kilometre scale, the numerical method would still run in under four minutes to compute the associated wildfire evolution on the order of days.

6. Conclusion

Wildfire spread, spotfire merger and the effect of firebreaks have been modelled in this work using a simple, two-dimensional model. This model could then successfully capture the main features of wildfire spread: the development of the fire line into a parabolic shape; the closing of the V-gap in junction fires; and the attraction of two wildfires towards each other. The wildfire spread itself is dependent on three main effects: the basic rate of spread divided explicitly into its radiative and convective components; the ambient wind; and the pyrogenic wind — a self induced wind caused by the updraft created by the wildfire over its burnt region. While in this model the ambient wind and basic

ROS effects are purely kinematical and prescribed by given constants, the pyrogenic wind is determined by the solution of Laplace's equation in the wildfire exterior. Two numerical methods which compute the fire line evolution have been developed.

The first method is exclusively used for single wildfire scenarios and involves finding a numerical approximation of the conformal map from the fire line exterior to the exterior of the fixed unit disk in an auxiliary plane. The problem is reduced to a PG-type equation for the unknown conformal map f, which, when expressed as a truncated Laurent series, reduces to a system of n ODEs for the unknown coefficients. The second method is capable of computing the evolution of multiple wildfires and calculates the pyrogenic potential ϕ directly in the physical plane by means of the AAA-LS algorithm (Costa and Trefethen, 2023). This involves a rational approximation of the pyrogenic potential involving singularities in the (unphysical) burnt region, which can then be solved by means of a simple least-squares method for given boundary data. Unlike the conformal mapping method, the AAA-LS algorithm is explicitly employed at each time step and so an RK timestepping method is used to compute the evolution of the wildfire. Additionally, the multiple wildfire method can handle fire mergers, with the MATLAB *union* function used to combine two overlapping fire lines into one, connected curve.

The methods developed here have further scope for improvement, advancement and extension — some possible extensions are now discussed.

Topography and terrain effects have been ignored in this work yet can play as crucial a role in wildfire spread as the effect of wind. The influence of terrain can be included simply into the wildfire spread Eq. (11) but care is needed in how slopes and valleys would affect the exterior wind field. As suggested in Sharples and Hilton (2020), an analogue to terrain could be the inclusion of vortices which reproduce terrain effects on the wildfire spread such as vorticity-driven lateral spread. The inclusion of sources, sinks and point vortices into the exterior wind field could additionally be used to model other wildfire features such as fire whirls and tornadoes (Soma and Saito, 1991; Forthofer and Goodrick, 2011; Tohidi et al., 2018; Lareau et al., 2022). As stated in Section 4.4, inhomogeneous fuel beds could also be incorporated into the model in a similar manner to the firebreak wildfire Eq. (26); it would then be simple to couple some existing fuelbed database into the model. Other factors could also be included in Eq. (11), for example how oxygen availability and transport affects the wildfire spread (Zik and Moses, 1999; Harris and McDonald, 2022).

Furthermore, the merging algorithm could be adapted to allow for more complicated merging scenarios. For example, multiple wildfires may merge in such a way that produces a ring fire – see figure 4.6 in Sharples et al. (2022) – which results in two disconnected 'inner and outer' unburnt domains. Locally, the opposite scenario may also appear where a 'doughnut' of unburnt fuel with a small fire at its centre is surrounded by a large outer fire on all sides. The AAA-LS algorithm can be extended to account for these types of domains (Trefethen, 2020; Costa and Trefethen, 2023). In addition, further consideration can be given to the plume strength of each wildfire and of a merged fire. In this work, it is assumed that each fire plume is of equal strength; following a merger, the new wildfire also generates a plume of the same strength as the previous two fires. A mechanism could be included which calculates the plume strength of a merged wildfire given the strengths of its constituent fires and which provides a time varying plume strength related to the size of the wildfire.

Finally, the current model is entirely deterministic yet wildfire spread, particularly in extreme weather conditions, is often stochastic. Thus stochastic variables could be incorporated into the model, for example an ambient wind with time-varying direction and magnitude or some variability on the basic ROS terms corresponding to stochastic heat fluxes. Another stochastic wildfire feature is the production and distribution of spotfires as a result of firebrand ejection from a main fire. In this work, the production of spotfires was not considered, rather it was assumed they were present as mature, independent wildfires. The model of this work could be coupled with a stochastic spotfire generation model, for example similar to that in Boychuk et al. (2009), such that spotfires could appear midway through a scenario and affect the wildfire spread thereafter.

CRediT authorship contribution statement

Samuel J. Harris: Writing – review & editing, Writing – original draft, Visualization, Validation, Software, Methodology, Investigation, Conceptualization. **N.R. McDonald:** Writing – review & editing, Supervision, Methodology, Investigation, Conceptualization.

Declaration of competing interest

The authors declare the following financial interests/personal relationships which may be considered as potential competing interests: Samuel Joseph Harris reports financial support was provided by the UK Engineering and Physical Sciences Research Council. Some images from the results of Hilton et al. (2018) and the associated experiments of Sullivan et al. (2019) have been used in this work, with agreement from the authors of the original cited works. If there are other authors, they declare that they have no known competing financial interests or personal relationships that could have appeared to influence the work reported in this paper.

Acknowledgements

The authors thank James Hilton, Jason Sharples, Andrew Sullivan, William Swedosh and their team for allowing the use of both their experimental fire data from the CSIRO Pyrotron and the simulation outputs from the pyrogenic potential model in this work. Please see their associated works Hilton et al. (2018) and Sullivan et al. (2019). The authors also thank the anonymous reviewers for their useful comments and suggestions. Samuel J. Harris was supported by a UK Engineering and Physical Sciences Research Council Ph.D. studentship, Grant No. EP/N509577/1 and EP/T517793/1.

Data availability

All code used in this work is made publically available via the link in the article.

References

Achtemeier, G.L., 2012. Field validation of a free-agent cellular automata model of fire spread with fire–atmosphere coupling. Int. J. Wildland Fire 22, 148–156.
Amano, K., 1994. A charge simulation method for the numerical conformal mapping of interior, exterior and doubly-connected domains. J. Comput. Appl. Math. 53, 353–370.
Ambroz, M., Balažovjech, M., Medl'a, M., Mikula, K., 2019. Numerical modeling of wildland surface fire propagation by evolving surface curves. Adv. Comput. Math. 45, 1067–1103.
Andrews, P., 2018. The Rothermel Surface Fire Spread Model and Associated Developments: A Comprehensive Explanation, vol. 371. Gen. Tech. Rep. RMRS-GTR-371. Fort Collins, CO: US Department of Agriculture, Forest Service, Rocky Mountain Research Station, p. 121.
Arnell, N.W., Freeman, A., Gazzard, R., 2021. The effect of climate change on indicators of fire danger in the UK. Environ. Res. Lett. 16, 044027.
Attiwill, P., Binkley, D., 2013. Exploring the mega-fire reality: A 'forest ecology and management' conference. For. Ecol. Manag. 294, 1–3.
Ausonio, E., Bagnerini, P., Ghio, M., 2021. Drone swarms in fire suppression activities: A conceptual framework. Drones 5, 17.
Baines, P.G., 1990. Physical mechanisms for the propagation of surface fires. Math. Comp. Model. 13, 83–94.
Bakhshaii, A., Johnson, E.A., 2019. A review of a new generation of wildfire–atmosphere modeling. Can. J. Res. 49, 565–574.
Bazant, M.Z., Crowdy, D., 2005. Conformal mapping methods for interfacial dynamics. In: Handbook of Materials Modeling. Springer, pp. 1417–1451.

Bebieva, Y., Oliveto, J., Quaife, B., Skowronski, N.S., Heilman, W.E., Speer, K., 2020. Role of horizontal eddy diffusivity within the canopy on fire spread. Atmosphere 11, 672.

Beer, T., 1991. The interaction of wind and fire. Bound.-Layer Meteorol. 54, 287–308.

Bonta, M., Gosford, R., Eussen, D., Ferguson, N., Loveless, E., Witwer, M., 2017. Intentional fire-spreading by "Firehawk" raptors in Northern Australia. J. Ethnobiol. 37, 700–718.

Boychuk, D., Braun, W.J., Kulperger, R.J., Krougly, Z.L., Stanford, D.A., 2009. A stochastic forest fire growth model. Environ. Ecol. Stat. 16, 133–151.

Brown, J.W., Churchill, R.V., 2009. Complex Variables and Applications, eighth ed. McGraw-Hill.

Brubeck, P.D., Nakatsukasa, Y., Trefethen, L.N., 2021. Vandermonde with Arnoldi. SIAM Rev. 63, 405–415.

Butcher, J.C., 1996. A history of Runge-Kutta methods. Appl. Numer. Math. 20, 247–260.

Canós, A.J., 2024. Fast and robust self-intersections (version 1.0.0.0) [software], MATLAB Central File Exchange. Retrieved August 1, 2024. URL: https://www.mathworks.com/matlabcentral/fileexchange/13351-fast-and-robust-self-intersections.

Catchpole, E.A., Hatton, T.J., Catchpole, W.R., 1989. Fire spread through nonhomogeneous fuel modelled as a Markov process. Ecol. Model. 48, 101–112.

Clark, T.L., Jenkins, M.A., Coen, J., Packham, D., 1996a. A coupled atmosphere-fire model: Convective feedback on fire-line dynamics. J. Appl. Meteorol. Climatol. 35, 875–901.

Clark, T.L., Jenkins, M.A., Coen, J.L., Packham, D.R., 1996b. A coupled atmosphere-fire model: Role of the convective Froude number and dynamic fingering at the fireline. Int. J. Wildland Fire 6, 177–190.

Costa, S., 2020. Solving Laplace problems with the AAA algorithm. arXiv preprint arXiv:2001.09439.

Costa, S., Trefethen, L., 2023. AAA-least squares rational approximation and solution of Laplace problems. In: European Congress of Mathematics. pp. 511–534.

Dallaston, M.C., McCue, S.W., 2013. An accurate numerical scheme for the contraction of a bubble in a Hele–Shaw cell. ANZIAM J. 54, C309–C326.

Dallaston, M.C., McCue, S.W., 2016. A curve shortening flow rule for closed embedded plane curves with a prescribed rate of change in enclosed area. Proc. R. Soc. A 472, 20150629.

D'Errico, J., 2024. Interparc (version 1.3.0.0) [software], MATLAB Central File Exchange. Retrieved August 1, 2024. URL: https://www.mathworks.com/matlabcentral/fileexchange/34874-interparc.

Dipierro, S., Valdinoci, E., Wheeler, G., Wheeler, V.-M., 2024. A simple but effective bushfire model: analysis and real-time simulations. SIAM J. Appl. Math. 84, 1504–1514.

Driscoll, T.A., 2005. Algorithm 843: Improvements to the Schwarz-Christoffel toolbox for MATLAB. ACM Trans. Math. Software 31, 239–251.

Driscoll, T.A., Trefethen, L.N., 2002. Schwarz-Christoffel Mapping, vol. 8. Cambridge University Press.

Dritschel, D.G., 1988. Contour surgery: a topological reconnection scheme for extended integrations using contour dynamics. J. Comput. Phys. 77, 240–266.

Entov, V.M., Etingof, P.I., 1991. Bubble contraction in Hele-Shaw cells. Q. J. Mech. Appl. Math. 44, 507–535.

Filippi, J.-B., Bosseur, F., Pialat, X., Santoni, P.-A., Strada, S., Mari, C., 2011. Simulation of coupled fire/atmosphere interaction with the MesoNH-ForeFire models. J. Combust. 2011, 540390.

Finney, M., 1998. FARSITE, Fire Area Simulator–model development and evaluation (No. 4). US Department of Agriculture, Forest Service, Rocky Mountain Research Station.

Fons, W.L., 1946. Analysis of fire spread in light forest fuels. J. Agric. Res. 72, 92–121.

Forthofer, J.M., Goodrick, S.L., 2011. Review of vortices in wildland fire. J. Combust. 1, 984363.

Goldstein, M.E., Reid, R.L., 1978. Effect of fluid flow on freezing and thawing of saturated porous media. Proc. Roy. Soc. A. 364, 45–73.

Gopal, A., Trefethen, L.N., 2019a. Representation of conformal maps by rational functions. Numer. Math. 142, 359–382.

Gopal, A., Trefethen, L.N., 2019b. Solving Laplace problems with corner singularities via rational functions. SIAM J. Num. Anal. 57, 2074–2094.

Grodzki, P., Szymczak, P., 2019. Reactive-infiltration instability in radial geometry: From dissolution fingers to star patterns. Phys. Rev. E 100, 033108.

Gustafsson, B., Vasil'ev, A., 2006. Conformal and Potential Analysis in Hele-Shaw Cells. Springer Science & Business Media.

Harris, S.J., McDonald, N.R., 2022. Fingering instability in wildfire fronts. J. Fluid Mech. 943, A34.

Harris, S.J., McDonald, N.R., 2023. Penguin huddling: a continuum model. Acta Appl. Math. 185, 7.

Hetzer, J., Forrest, M., Ribalaygua, J., Prado-López, C., Hickler, T., 2024. The fire weather in Europe: large-scale trends towards higher danger. Environ. Res. Lett. 19, 084017.

Hilton, J., Garg, N., 2021. Rapid wind–terrain correction for wildfire simulations. Int. J. Wildland Fire 30, 410–427.

Hilton, J.E., Miller, C., Sharples, J.J., Sullivan, A.L., 2016. Curvature effects in the dynamic propagation of wildfires. Int. J. Wildland Fire 25, 1238–1251.

Hilton, J.E., Sullivan, A.L., Swedosh, W., Sharples, J., Thomas, C., 2018. Incorporating convective feedback in wildfire simulations using pyrogenic potential. Environ. Model. Softw. 107, 12–24.

Hu, X., Sun, Y., 2007. Agent-based modeling and simulation of wildland fire suppression. In: 2007 Winter Simulation Conference. IEEE, pp. 1275–1283.

Izhaki, I., Adar, M., 1997. The effects of post-fire management on bird community succession. Int. J. Wildland Fire 7, 335–342.

Jolly, W.M., Cochrane, M.A., Freeborn, P.H., Holden, Z.A., Brown, T.J., Williamson, G.J., Bowman, D.M., 2015. Climate-induced variations in global wildfire danger from 1979 to 2013. Nature Commun. 6, 7537.

Kaur, I., Mentrelli, A., Bosseur, F., Filippi, J.-B., Pagnini, G., 2016. Turbulence and fire-spotting effects into wild-land fire simulators. Commun. Nonlinear Sci. Numer. Simul. 39, 300–320.

Khan, N., Sutherland, D., Moinuddin, K., 2023. Simulated behaviour of wildland fire spreading through idealised heterogeneous fuels. Int. J. Wildland Fire 32, 738–748.

Ladd, A.J.C., Yu, L., Szymczak, P., 2020. Dissolution of a cylindrical disk in Hele-Shaw flow: a conformal-mapping approach. J. Fluid Mech. 903, A46.

Lareau, N.P., Clements, C.B., 2017. The mean and turbulent properties of a wildfire convective plume. J. Appl. Meteorol. Climatol. 56, 2289–2299.

Lareau, N.P., Nauslar, N.J., Bentley, E., Roberts, M., Emmerson, S., Brong, B., Mehle, M., Wallman, J., 2022. Fire-generated tornadic vortices. Bull. Am. Meteorol. Soc. 103, E1296–E1320.

Linn, R., Reisner, J., Colman, J., Winterkamp, J., 2002. Studying wildfire behavior using FIRETEC. Int. J. Wildland Fire 11, 233–246.

Liu, N., Lei, J., Gao, W., Chen, H., Xie, X., 2021. Combustion dynamics of large-scale wildfires. Proc. Combust. Inst. 38, 157–198.

Malangone, L., Russo, P., Vaccaro, S., 2011. Effects of wind and terrain slope on flames propagation in a vegetative fuel bed. In: Submitted to the XXXIV Event of the Italian Section of the Combustion Institute (2011).

Mallet, V., Keyes, D.E., Fendell, F.E., 2009. Modeling wildland fire propagation with level set methods. Comput. Math. Appl. 57, 1089–1101.

Mandel, J., Beezley, J.D., Kochanski, A.K., 2011. Coupled atmosphere-wildland fire modeling with WRF 3.3 and SFIRE 2011. Geosci. Model Dev. 4, 591–610.

Markstein, G.H., 1951. Experimental and theoretical studies of flame-front stability. J. Aeronaut. Sci. 18, 199–209.

Martin, J., Hillen, T., 2016. The spotting distribution of wildfires. Appl. Sci. 6, 177.

Masson-Delmotte, V., Zhai, P., Pirani, A., Connors, S.L., Péan, C., Berger, S., Caud, N., Chen, Y., Goldfarb, L., Gomis, M.I., Huang, M., Leitzell, K., Lonnoy, E., Matthews, J.B.R., Maycock, T.K., Waterfield, T., ci, O.Y., Yu, R., Zhou, B. (Eds.), 2021. IPCC, 2021: Climate Change 2021: The Physical Science Basis. Contribution of Working Group I to the Sixth Assessment Report of the Intergovernmental Panel on Climate Change. Cambridge University Press.

McDonald, N.R., Harris, S.J., 2024. Exact and numerical solutions of a free boundary problem with a reciprocal growth law. IMA J. Appl. Math. 89, 374–386.

Mell, W., Jenkins, M.A., Gould, J., Cheney, P., 2007. A physics-based approach to modelling grassland fires. Int. J. Wildland Fire 16, 1–22.

Miller, C., Hilton, J., Sullivan, A., Prakash, M., 2015. SPARK–a bushfire spread prediction tool. In: International Symposium on Environmental Software Systems. Springer, pp. 262–271.

Morvan, D., Accary, G., Meradji, S., Frangieh, N., 2022. Fifty years of progress in wildland fire modelling: from empirical to fully physical CFD models. C.R. Mécanique 350, 1–9.

Nakatsukasa, Y., Sète, O., Trefethen, L.N., 2018. The AAA algorithm for rational approximation. SIAM J. Sci. Comput. 40, A1494–A1522.

Nakatsukasa, Y., Sete, O., Trefethen, L.N., 2023. The first five years of the AAA algorithm. arXiv preprint arXiv:231203565.

Osher, S., Sethian, J.A., 1988. Fronts propagating with curvature-dependent speed: Algorithms based on Hamilton-Jacobi formulations. J. Comput. Phys. 79, 12–49.

Papadopoulos, G.D., Pavlidou, F.N., 2011. A comparative review on wildfire simulators. IEEE Syst. J. 5, 233–243.

Pastor, E., Zárate, L., Planas, E., Arnaldos, J., 2003. Mathematical models and calculation systems for the study of wildland fire behaviour. Prog. Energy Combust. Sci. 29, 139–153.

Quaife, B., Speer, K., 2021. A simple model for wildland fire Vortex–Sink interactions. Atmosphere 12, 1014.

Ribeiro, C., Viegas, D.X., Raposo, J., Reis, L., Sharples, J., 2023. Slope effect on junction fire with two non-symmetric fire fronts. Int. J. Wildland Fire 32, 328–335.

Rothermel, R.C., 1972. A Mathematical Model for Predicting Fire Spread in Wildland Fuels, vol. 115. Intermountain Forest & Range Experiment Station, Forest Service, US Department of Agriculture, 1972..

Rycroft, C.H., Bazant, M.Z., 2016. Asymmetric collapse by dissolution or melting in a uniform flow. Proc. Roy. Soc. A 472, 20150531.

Santoni, P.A., Bartoli, P., Simeoni, A., Torero, J., 2014. Bulk and particle properties of pine needle fuel beds–influence on combustion. Int. J. Wildland Fire 23, 1076–1086.

Sethian, J.A., 1985. Curvature and the evolution of fronts. Comm. Math. Phys. 101, 487–499.

Sethian, J.A., 2001. Evolution, implementation, and application of level set and fast marching methods for advancing fronts. J. Comput. Phys. 169, 503–555.

Sharples, J.J., Hilton, J.E., 2020. Modeling vorticity-driven wildfire behavior using near-field techniques. Front. Mech. Eng. 5, 69.

Sharples, J.J., Hilton, J.E., Badlan, R.L., Thomas, C.M., McRae, R.H.D., 2022. Fire line geometry and pyroconvective dynamics. In: Speer and Goodrick (2022). Cambridge University Press. pp. 77–128.

Sharples, J., Towers, I., Wheeler, G., Wheeler, V.-M., McCoy, J.A., 2013. Modelling fire line merging using plane curvature flow. In: 20th International Congress on Modelling and Simulation. Adelaide, Australia, pp. 256–262.

Smith, R.K., Morton, B.R., Leslie, L.M., 1975. The role of dynamic pressure in generating fire wind. J. Fluid Mech. 68, 1–19.

Soma, S., Saito, K., 1991. Reconstruction of fire whirls using scale models. Combust. Flame 86, 269–284.

Speer, K., Goodrick, S., 2022. Wildland fire dynamics: Fire effects and behavior from a fluid dynamics perspective. Wildland Fire Dynamics: Fire Effects and Behavior from a Fluid Dynamics Perspective. Cambridge University Press.

Sullivan, A., 2009. Wildland surface fire spread modelling, 1990–2007. 1: Physical and quasi-physical models. Int. J. Wildland Fire 18, 349–368.

Sullivan, A.L., 2022. Wildland fire combustion dynamics: The intersection of combustion chemistry and fluid dynamics. In: Speer and Goodrick (2022). Cambridge University Press. pp. 1–34.

Sullivan, A.L., Swedosh, W., Hurley, R.J., Sharples, J.J., Hilton, J.E., 2019. Investigation of the effects of interactions of intersecting oblique fire lines with and without wind in a combustion wind tunnel. Int. J. Wildland Fire 28, 704–719.

Sun, R., Krueger, S.K., Jenkins, M.A., Zulauf, M.A., Charney, J.J., 2009. The importance of fire–atmosphere coupling and boundary-layer turbulence to wildfire spread. Int. J. Wildland Fire 18, 50–60.

Thomas, C.M., Sharples, J.J., Evans, J.P., 2017. Modelling the dynamic behaviour of junction fires with a coupled atmosphere–fire model. Int. J. Wildland Fire 26, 331–344.

Tohidi, A., Gollner, M.J., Xiao, H., 2018. Fire whirls. Annu. Rev. Fluid Mech. 50, 187–213.

Trefethen, L.N., 2018. Series solution of Laplace problems. ANZIAM J. 60, 1–26.

Trefethen, L.N., 2020. Numerical conformal mapping with rational functions. Comp. Meth. Funct. Theor. 20, 369–387.

Trelles, J., Pagni, P., 1997. Fire-induced winds in the 20 October 1991 Oakland Hills fire. Fire Saf. Sci. 5, 911–922.

Urban, J.L., Song, J., Santamaria, S., Fernandez-Pello, C., 2019. Ignition of a spot smolder in a moist fuel bed by a firebrand. Fire Saf. J. 108, 102833.

Viegas, D.X., Raposo, J.R., Davim, D.A., Rossa, C.G., 2012. Study of the jump fire produced by the interaction of two oblique fire fronts. Part 1. Analytical model and validation with no-slope laboratory experiments. Int. J. Wildland Fire 21, 843–856.

Weber, R., 1991. Modelling fire spread through fuel beds. Prog. Energy Combust. Sci. 17, 67–82.

Wheeler, V.M., Wheeler, G.E., McCoy, J.A., Sharples, J., 2015. Modelling dynamic bush-fire spread: perspectives from the theory of curvature flow. In: 21st International Congress on Modelling and Simulation. Gold Coast, Australia, pp. 319–325.

Xue, B.B., Johnson, E.R., McDonald, N.R., 2017. New families of vortex patch equilibria for the two-dimensional Euler equations. Phys. Fluids 29. 12 (2017).

Yfantidou, A., Zoka, M., Stathopoulos, N., Kokkalidou, M., Girtsou, S., Tsoutsos, M.-C., Hadjimitsis, D., Kontoes, C., 2023. Geoinformatics and machine learning for comprehensive fire risk assessment and management in peri-urban environments: A building-block-level approach. Appl. Sci. 13, 10261.

Zik, O., Moses, E., 1999. Fingering instability in combustion: An extended view. Phys. Rev. E 60, 518–531.